國立臺灣大學理學院海洋研究所
碩士論文
Institute of Oceanography
College of Science
National Taiwan University
Master Thesis

利用拖曳式發收器於淺海環境聲測流研究

Shallow-Water Acoustic Mapping of Ocean Currents Using Towed Transceivers

李允文
Yun-Wen Li

指導教授：黃千芬 博士
Advisor: Chen-Fen Huang, Ph.D.

中華民國 105 年 8 月
August, 2016

10.6342/NTU201603287

致謝

本研究的完成，我首先感謝指導教授黃千芬老師，感謝老師給我在研究、寫作、學業和各式技能方面上給予專業且孜孜不倦的指導。老師總是一絲不苟的指導學生，精心的準備課程，指引我在浩瀚學海中找到方向，讓我學習去深入思考一個現象或是文獻中一段文字背後所隱含的深刻意涵。我在此表達誠心的感激。

同時，我要感謝劉金源教授、郭振華教授、黃清哲教授與谷口直和博士百忙之中來擔任我的論文口試委員。 委員們細心地檢驗我的研究，點出了其中的盲點與不足，同時對本研究給予寶貴的建議，使得研究更趨完善。 委員們提出的問題，讓我重新思索此研究與其他相關研究的聯繫。

我要感謝海洋所的老師們給予我在研究上許多珍貴的建議，老師們在課堂上及青年論壇中對我提出的問題，都是提供我一個新的視角來檢視我的研究；除了研究上，也感謝老師們在各個課程上的用心，帶領我走入知識的殿堂。

我要感謝海研三號研究船上的工作人員在實驗上的各種幫助及指導。我要感謝貴儀中心的謝祥志，王弼，何文華技術員在實驗上的協助。 我要感謝海洋所的張宏毅技術師，給予我在實驗儀器上的諸多協助與指導。我要感謝水下載具實驗室的學長及同學在實驗上的幫助。

我要感謝彥翔、士傑、康淵和建文，四位學長傳授給我研究上、電腦程式上、課程上的珍貴經驗，感謝學長們付出寶貴時間與我討論研究相關的問題。我要感謝實驗室的同伴們——政緯及凱富——給我研究上和日常生活上的協助，也祝福你們的研究順利進行。我要感謝物理組的同學爲我加油打氣。我要感謝張淑惠女士和百晴助理在行政業務上的幫助，也感謝海洋所的行政人員在各種事務上的協助。

最後，我要感謝親人給我的支持。感謝文琪給我的鼓勵和陪伴。感謝我的父母和家人給我一個幸福溫暖的家。

2016年8月17日

10.6342/NTU201603287

中文摘要

本研究在淺海環境下使用四個固定式和一個拖曳式聲波發收器，以實現移動載具水聲流場測繪的技術。水聲流場測繪的原理是基於聲波在一測線上來回走時差與流場沿著聲線方向上的積分成正比，因此可以藉由在不同測線上聲波來回走時差來估算流場。若使用拖曳式測站，除了其運動將影響來回走時差，因相對運動影響所造成的都普勒效應，將會使訊號發生失眞的現象。利用所發射的M序列訊號對都普勒頻移變化的敏感性，藉由時間延遲-都普勒模糊函數的方法，由估算都普勒頻移量推算測站間的相對速度，同時以此都普勒頻移量補償接收訊號的失眞。由於水聲通道多重路徑的效應，傳統以配對來回波形峰值到時估算走時差的方法，因不同路徑之聲線相互干擾，此方法易產生誤差。本研究提出一基於來回波形之交互相關函數隨時間變化的關係以追蹤來回走時差。理想情況下，訊號來回走時差可由相關函數最大值所對應的延遲作爲估計；但因多重路徑干擾，來回訊號的相關函數經常存在多個相關係數相近的峰值。本研究利用相關函數的時間序列，以選擇合適的峰值來估算來回走時差。藉由2015年9月在西子灣海洋實驗場蒐集的資料，以估算當地的二維流場。藉由拖曳式測站所收集的聲學資料經過訊號處理後提高可用的聲線量。拖曳式測站和和固定式測站間的聲線以各種角度掃描水體，同時也增加了流場測繪的範圍。這些聲線上的走時差除了用於估算流場，以可檢驗估算的流場。實驗場址的流場型態以半日潮流爲主，其主軸平行於地形等深線。資料分析結果顯示，運用聲學流場測繪技術所估算下的流速隨時間的變化與船載式都普勒流速儀的量測一致，並且所重建的二維流場也展示了在流向改變時，流場分佈有明顯的空間變異。

關鍵字：水聲層析法，聲學監測，都普勒效應，來回走時差

10.6342/NTU201603287

Abstract

This study uses four moored acoustic transceivers (a device consisting of a source and a receiver) along with one towed by a ship to demonstrate the acoustic mapping of ocean currents with the mobile station in a shallow-water environment. The basic principle of the acoustic mapping for currents is that the difference in the travel times (DTT) of oppositely traveling acoustic signals is proportional to the integrated current velocity along the acoustic ray path. Thus the currents can be estimated with the DTT data. When the towed transceiver is incorporated, the acoustic signal is Doppler-distorted and the DTTs are affected due to the relative instrument motion. Since the transmitted signal, m-sequence, is highly sensitive to Doppler, the method based upon the delay-Doppler ambiguity function can determine the Doppler shift and the arrival patterns simultaneously. For the estimation of DTT, the conventional approach using the peak-picking method is subject to the uncertainties in identifying and resolving acoustic rays in the shallow-water environment. Hence, this study proposed a method based on the cross-correlation function (CCF) of the reciprocal arrival patterns. Ideally, the DTT could be obtained by the lag time corresponding to the maximum correlation. However, due to the multiple acoustic arrivals the CCF exhibits multiple peaks with similar heights. To address this issue, we utilize the time-evolving CCFs to select appropriate peaks for the determination of DTT. Using the data collected at Sizhiwan Marine Test Field, Kaohsiung, in September of 2015, the current field was estimated. The towed transceiver in the experiment provided additional reciprocal travel-time data for sensing the water volume at many angles and increased the coverage of the mapping area. Besides augmenting the number of DTT data for the current estimate, some of the data from the towed transceiver are used to validate the estimated field. The experiment site is dominated by the semi-diurnal tidal currents with the principal current direction flowing along the isobaths. The time evolution of the estimated current agrees well with the shipboard-ADCP measurements, and the spatial variations are observed when the currents change the direction.

Key words: Ocean acoustic tomography, acoustic monitoring, Doppler effect, differential travel time

10.6342/NTU201603287

Contents

10.6342/NTU201603287

10.6342/NTU201603287

List of Figures

10.6342/NTU201603287

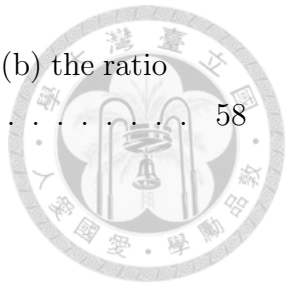

10.6342/NTU201603287

List of Tables

10.6342/NTU201603287

10.6342/NTU201603287

Chapter 1

Introduction

1.1 Background and Motivation

Monitoring the ocean may require much time and resources because the ocean is highly variable in time and space. For the point-measurement instruments, many sensors are needed to sense the ocean. The remote-sensing techniques, such as the satellites and high-frequency Radars, can provide a synoptic view of the ocean surface. However, it is difficult for these techniques to measure the interior properties of the ocean because of the high attenuation of the electromagnetic waves in sea water. The sound waves can propagate in the ocean efficiently. Compared to other types of waves, sound with low attenuation (especially low-frequency one) can travel a long distance in the ocean [17]. Also, due to its high propagation speed of about 1,500 $\mathrm{m\,s^{-1}}$, it is possible for the acoustic wave to pass through the area of hundreds of kilometers within minutes.

Ocean acoustic tomography (OAT), which takes full advantages of the sound, was proposed to monitor the interior structure of the ocean using the acoustic method. With the precise acoustic measurements and the knowledge of the sound propagation in the ocean, it is possible to probe the interior of the water mass in the ocean using the acoustic waves. Although not limited to, the travel-times usually are the primary acoustic measurements for their robustness over the long-distance acoustic transmission. The travel time of an acoustic pulse traversing from the source to receiver provides the measures for the integrals of the sound speed and current velocity along the ray path. Given the precise travel-time data from multiple acoustic paths, the sound speed or current velocity field can be reconstructed. Instead of directly measuring the ocean properties, the OAT technique requires solving an inversion problem to infer for the ocean properties from the measurements.

10.6342/NTU201603287

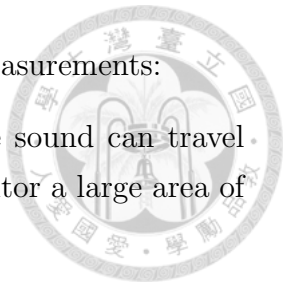

The technique offers several advantages over the conventional measurements:

1. The technique provides synoptic measurements. Since the sound can travel long distances with a high speed, it is thus possible to monitor a large area of the ocean with a short period.

2. The technique provides spatially-integrated measurements. The acoustic data provide integral measures of the ocean properties along the ray path. These data may reduce the measurement noise from the fine structure of the ocean feature. The integral data are direct measurements of the mass transport and heat content.

3. The instruments can be deployed outside the area of interest. It is sometimes difficult to deploy the instruments in the area of study. Inherently OAT is a remote-sensing technique, and the tomographic systems can be deployed at the exterior of the study area.

Data density is an important factor that determines the effectiveness of acoustic mapping using the travel-time data. Moving ship tomography (MST) was proposed to increase the ray paths (the quantity of data) by incorporating the mobile sources and/or receivers. The ray paths between the mobile and moored transceivers can propagate through the ocean at various angles and increase the sampling coverage. The idea of mobile transceivers has not been realized in the small-scale coastal ocean. One purpose of this study is to evaluate the feasibility of incorporating the towed transceivers in the acoustic mapping.

The development of OAT in the shallow water came later than that in the deep sea due to the complicated acoustic propagation in the shallow water waveguide. Individual acoustic arrivals may not be resolved due to the multipath interference, and the ray identification is difficult to conduct because of the channel complexity. But given the frequently transmitted acoustic data, it is still possible to identify the evolution pattern of the environment from the random fluctuations.

It is perhaps better to distinguish the study here from OAT by referring itself to as acoustic mapping. While OAT puts much emphasis on the inverse problems, this study uses simplified formulations to relate the acoustic measurements to the physical ocean properties (currents), bypassing the complicated inversion process and the ray identification problems. The motivation for the simplification is that the characteristics of the sound propagation (forward problem) are complicated in the shallow water, which is different from the deep-sea environments where many OAT experiments conducted. This study aims to map the ocean currents in the

10.6342/NTU201603287

shallow water using the acoustic travel-time data featuring the usage of the towed transceivers.

1.2 A Concise Survey of Literature

OAT proposed by Munk and Wunsch [16] is a method for remote sensing of the ocean interior. Observing the time-evolving mesoscale features of the ocean interior is a challenging task. It would require many research ships or many moorings deployed simultaneously to fully survey the area. Using the OAT technique, it is possible to map a large area of the water mass with a set of the acoustic sources and receivers (referred to as transceivers).

Ocean acoustic tomography in the deep sea

The Ocean Tomography Group conducted an experiment in 1981 to demonstrate the feasibility of OAT [1]. Four acoustic sources and five receivers were deployed in an area surrounded by a 300 km by 300 km region. The travel times of the acoustic rays traversed from the sources to the receivers were accurately measured. Also, the ray paths and the travel times of the rays can be well predicted using the climatological mean of the sound speed field. The predicted acoustic arrivals showed good agreement with the measured ones. The difference between the predicted and measured travel times is due to the perturbation of the sound speed fields. Using the existing inverse methods, the sound speed field was inferred from the travel-time data.

While the one-way travel times are used to estimate the sound speed fields, the difference between reciprocal travel times, referred to as differential travel times (DTTs), can be used to estimate the current velocity. Since the current velocity of the ocean (1 $\mathrm{m\,s^{-1}}$) is usually very small compared to the typical sound speed ranged from 1480 to 1540 $\mathrm{m\,s^{-1}}$ [40], the DTT is mainly affected by the current velocity along the ray path.

Worcester [34] successfully conducted an experiment of reciprocal acoustic transmission in a midocean environment. Two stations were deployed separated with a distance of 25 km. Each station was deployed from a research ship and consisted of an acoustic source and a receiving array. Two stations transmitted the acoustic signals simultaneously and recorded the acoustic data from the reciprocal transmission. The data of the reciprocal transmission can separate the current effect on the travel times from the sound speed perturbation. The DTTs, obtained from the reciprocal

pulse responses, are interpreted as the raypath-averaged current.

Moving ship tomography

Cornuelle *et al.* [3] proposed Moving Ship Tomography (MST) as a method of obtaining high-resolution, nearly synoptic maps of the ocean temperature or current field over large areas. The idea is to incorporate mobile stations. Using the acoustic rays between the ship-towed and moored transceivers passing through the ocean at various angles, the number of the rays increases with the number of the mobile acoustic transceiver.

The Acoustic Mid-Ocean Dynamics Experiment Group (AMODE) conducted a field experiment to demonstrate MST in 1991 [28]. The experiment was conducted in the North Atlantic Ocean with six transceiver moorings and one receiving array. The receiving array was circumnavigated at a radius of 500 km about two times over 51 days. The array was operated on a dip-and-run mode from a ship, yielding 120 stops along the circular course. In their preliminary results, the sound speed field was assumed to be frozen within a 15-day period (the ship had circumnavigated 60% of the circular course). The travel-time data from all the possible rays collected during the period were used to reconstruct the sound speed field using the tomographic inversion method. The reconstructed field [the area inside the circle in Figure 1.1(a)] agrees well with the *in-situ* measurements [the area inside the rectangular box in Figure 1.1(b)] and reveals the mesoscale feature of the ocean.

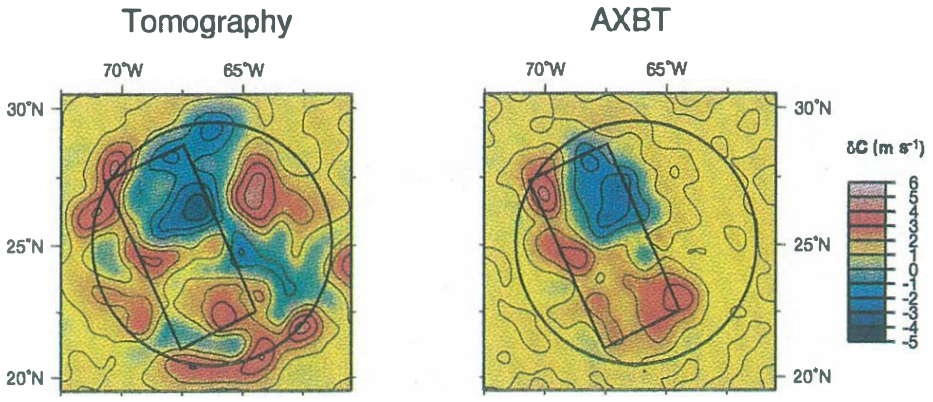

Figure 1.1: Results of the MST experiment in 1991 conducted by AMODE [28]. Sound speed perturbation at the depth of 700 m from the (a) tomographic results and (b) Airborne EXpendable BathyThermograph (AXBT).

10.6342/NTU201603287

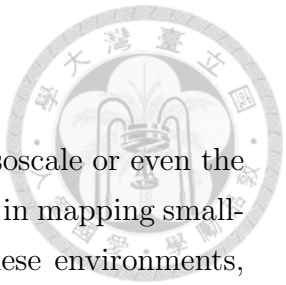

Coastal acoustic tomography

Although the original motivation of OAT was to monitor the mesoscale or even the basin-scale ocean, the OAT technique is also applicable and useful in mapping small-scale ocean features, such as the coastal seas and straits. In these environments, the characteristics of acoustic propagation are different from those in the deep sea. While much of the acoustic propagation can be well predicted in the deep sea , the acoustic propagation in shallow-water environments is affected by not only the ocean sound speeds but the seafloor geoacoustic properties as well as the bathymetry. In the shallow-water environment, the ray paths often involve the bounces from the sea bottom and/or from the sea surface. Thus, the propagation range is limited. For a short range sound propagation, the time spread for the multiple arrivals is small, resulting in the interference of different arriving rays. Therefore, individual arrivals may not be resolvable in the received arrival patterns.

Ko *et al.* [12] conducted a OAT experiment in the Florida Strait using three stations. The stations were bottom-mounted with the ranges of about 20 km. They reported the difficulties in resolving the travel times from the arrival patterns due to the ray interference. However, a strong signal, having a sharp falling edge and persistent in time, presents at the late portion of the arrival pattern . The travel time can then be obtained from that arrival. The estimated travel times were then used to estimate the current velocity, vorticity, and temperature. The results agree well with the direct measurements.

The current structure in the coastal waters can be complicated and contains the vortices in certain regions. It is sometimes not possible to fully survey these regions using the conventional instruments, such as acoustic Doppler current profilers (ADCPs) due to the heavy ship traffic or fisheries activities. The researcher group in Hiroshima University, Japan, began the research of Coastal Acoustic Tomography (CAT). The concept is to apply OAT in the coastal ocean. The CAT system can be deployed in the periphery of the experiment site (even deployed from the land in the appropriate site). The acoustic signals transmitted from the CAT systems then probe the area from the periphery.

Zheng *et al.* [38] conducted the experiment of the reciprocal sound transmission in Seto inland sea with two stations. Two stations were separately deployed from the ship with the distance of 5.7 km. From the reciprocal acoustic data, the path-averaged current was estimated using the obtained DTT. The estimated path-averaged current was consistent with the *in-situ* ADCP measurement. The CAT research continues with multiple stations, which can form many different ray paths.

The current (or sound speed) field in the region enclosed by the stations can be reconstructed using the acoustic data from these ray paths. Several CAT studies conducted by Hiroshima University [36, 37, 39] have proved the feasibility of resolving the complicated structure of the currents in the coastal ocean.

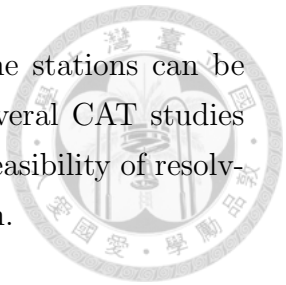

Recent studies of ocean acoustic tomography in Taiwan

Recently several OAT experiments are conducted by Acoustical Oceanography Laboratory (AOL), National Taiwan University, in the coastal waters surrounding Taiwan. The middle-range (about 50 km) OAT technique was applied to study the spatial and temporal variations of a sub-branch of the Kuroshio off the southeast coast of Taiwan with the joint effort of National Taiwan University and Hiroshima University [26]. The instruments were deployed near the sea floor off the strong flow of Kuroshio. Although the individual arrivals from the acoustic data were not resolved in this experiment, the arrivals were categorized into three groups corresponding to their ray paths. The DTT determined from each group provided a different depth-weighted current velocity. Therefore, the vertical profile of the currents was revealed from the data of those three arrival groups.

Huang *et al.* [9] conducted the reciprocal acoustic transmission in Bachimen Harbor, Keelung, Taiwan, with a very short transmission range of 490 m. The acoustic data contains multiple arrivals because the experiment site is a highly-reverberative environment for the acoustic wave. Two dominant acoustic arrivals were resolved from the data. Their corresponding ray paths, including a direct path and a horizontally reflected path from the side of the bank, were identified using the ray simulations. The path-averaged temperature and current velocity were estimated using the mean and the differential travel times, respectively.

Huang *et al.* [10] demonstrated the acoustic mapping of the currents using the distributed networked underwater sensors in Marine Test Field (MTF), Kaohsiung, Taiwan. Instead of deploying the instruments in the periphery following the conventional OAT/CAT practice, the stations were deployed within the water volume. The current vector in any place inside the mapping domain can be computed using the data from the neighboring stations. The developed algorithm for the current reconstruction is applied in this study. The algorithm does not involve the complicated computation (the tomographic inversion of the current field) and hence is suitable for the *in-situ* signal processing.

Recently, the research team of AOL conducted a feasibility test of moving vehicle tomography near the Sizihwan Bay in Kaohsiung, Taiwan, in 2015 [8]. Compared

10.6342/NTU201603287

with the dip-and-run mode operation used in the MST experiment by AMODE, the mobile station was towed continuously while conducting acoustic transmissions thanks to the lightweight of the instruments. This thesis carries out the acoustic mapping of currents using the data collected from this experiment.

1.3 Objectives

The objectives of this thesis included:

1. To apply Doppler processing techniques on the Doppler-distorted acoustic data to obtain the acoustic arrivals and the relative velocity of the instruments.
2. To estimate the DTT from the reciprocal acoustic transmission using the time series of cross-correlation functions.
3. To estimate the currents via the acoustic measurements and to validate the results.

1.4 Scopes of the Thesis

The major contents of this thesis consist of five chapters. Chapter 2 reviews the basic principles of acoustic mapping for the currents based on the acoustic travel-time data. The relevant techniques for obtaining the precise measurements, including the Doppler processing, pulse compression, modulation and the cross-correlation function are reviewed in this chapter. Chapter 3 describes the configuration of the field experiment and the instruments applied. Chapter 4 presents the process of extracting the parameters for the current mapping from the acoustic data collected in the reciprocal transmission. Chapter 5 presents the results and discussion, including the experimental data, the estimated currents and its error analysis, and the simulation of the acoustic ray path. The thesis is concluded with a summary and a suggestion of further development in Chapter 6.

10.6342/NTU201603287

Chapter 2

Theory

2.1 Path-Averaged Current Velocity and Differential Travel Time

This section reviews the basic principle of using the differential travel time (DTT) to estimate the currents [15]. Assuming a uniform current velocity ($\mathbf{v}$) in an ocean environment, two moving transceivers (Stations 1 and 2) transmit acoustic pulses reciprocally (Figure 2.1). In an infinite, homogeneous fluid the acoustic ray is a straight path connected between Stations 1 and 2. The travel times from Station 1 to Station 2, t_{12}, and from the reversed direction, t_{21}, can be represented as follows:

$$\begin{aligned} t_{12} &= \frac{R}{c + v_{\mathrm{m}} - u_2}, \\ t_{21} &= \frac{R}{c - v_{\mathrm{m}} + u_1}, \end{aligned} \tag{2.1}$$

where c is a reference sound-speed and R is the ray path length. To simplify the derivation $\mathbf{r}_{12}$ is defined as the unit vector along the ray path from Station 1 to Station 2. The variable $v_{\mathrm{m}} = \mathbf{v} \cdot \mathbf{r}_{12}$ is the current velocity along the ray path and $u_i = \mathbf{u}_i \cdot \mathbf{r}_{12}$ is the instrument velocity for the transceiver index i in the $\mathbf{r}_{12}$ direction.

In this study, the magnitudes of v_{m} (less than 1 $\mathrm{m\,s^{-1}}$) and u_i (about 1.5 $\mathrm{m\,s^{-1}}$) are much smaller than c (about 1540 $\mathrm{m\,s^{-1}}$), i.e., $|v_{\mathrm{m}}/c|$ and $|u_i/c|$ are in the order of 10^{-3}. Thus, the difference between the reciprocal travel times (t_{12} and t_{21}), Δt_{12}, can be approximated by:

$$\begin{aligned} \Delta t_{12} &= t_{12} - t_{21} \\ &\approx -\frac{2R}{c^2} v_{\mathrm{m}} + \frac{R}{c^2}(u_1 + u_2) \end{aligned} \tag{2.2}$$

10.6342/NTU201603287

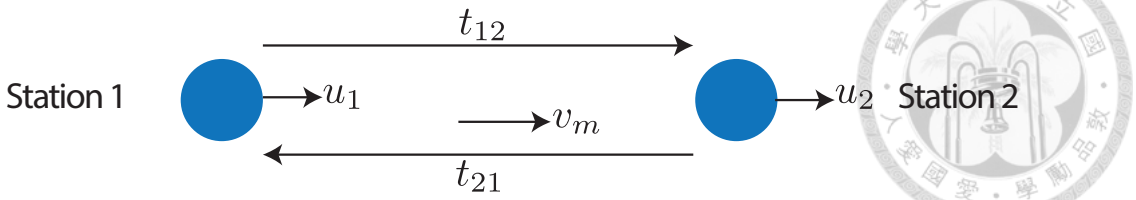

Figure 2.1: Reciprocal transmission between Stations 1 and 2.

The DTT is related to the path integral of the current velocity and the mean velocity of the two transceivers. Given the transceiver velocities, the current velocity v_{m} can be estimated using the DTT Δt_{12}. Unlike the one-way travel time (t_{12} or t_{21}) which is sensitive to the perturbations of R and c, Δt_{12} is less affected by the uncertainty in sound speed field as indicated in Equation (2.2) [34]. The discussion for the uncertainty in the estimated current, $\sigma_{v_{\mathrm{m}}}$, is provided in Section 5.4.

In this experiment the acoustic transmissions are either between a pair of moored stations or between the moored and towed stations. For the reciprocal transmission between a pair of the moored stations (Stations 1 and 2), the velocities u_1 and u_2 are approximated to zero and the current velocity v_{m} is estimated via

$$v_{\mathrm{m}} = -\frac{c^2 \Delta t_{12}}{2R}. \tag{2.3}$$

Whereas for the reciprocal transmission between a moored (stationary) station (Station 1) and a towed station (Station 2), the velocity of Station 1 (u_1) is negligible, i.e., $u_1 = 0$, and the velocity of Station 2 (u_2) can be thus represented by the relative velocity between two stations: $u_2 = -u_{\mathrm{r}}$. The negative sign is due to the different definitions of the velocity: u_{r} is positive when the stations move closer whereas u_2 is positive in the $\mathbf{r}_{12}$ direction. The relative velocity u_{r} can be estimated using the Doppler shift of the acoustic signal. The current velocity v_{m} can be estimated via

$$v_{\mathrm{m}} = -\frac{c^2 \Delta t_{12}}{2R} - \frac{u_{\mathrm{r}}}{2}. \tag{2.4}$$

The variables Δt_{12} and u_{r} in Equations (2.3) and (2.4) are the key parameters to be estimated from the experimental data. The methods for obtaining Δt_{12} and u_{r} can be found in Chapter 4 and Section 2.4, respectively. Note that Equations (2.3) and (2.4) are derived from the approximation made in Equation (2.2), which holds when $|v_{\mathrm{m}}/c|$ and $|u_i/c|$ are small.

The above discussion simplified the acoustic propagation in the underwater waveguide. The ray path was assumed to be the direct path (Path A in Figure

10.6342/NTU201603287

2.2). In reality, there usually exist multiple arrivals with different ray paths, and the ray paths are determined by the sound speed structure. Sound refracts when the sound-speed gradient is present. Also, there may exist bounces with the top and bottom interfaces. Path B (Figure 2.2) shows a ray path reflecting from boundaries.

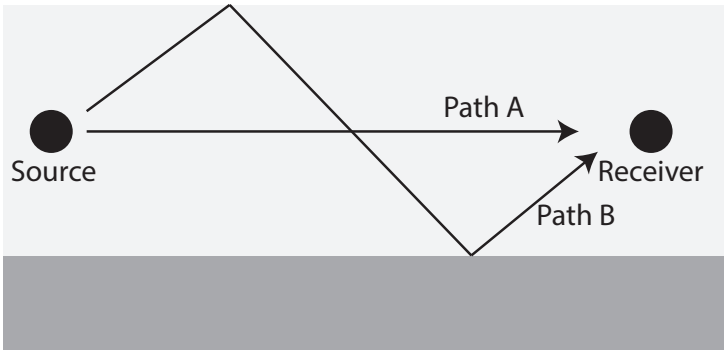

Figure 2.2: Multipath propagation in the waveguide. Path A denotes the direct path, and Path B denotes the path reflecting from the surface and bottom.

Next, we review the estimation of the path-averaged current when the ray path is not a straight line. Assuming an ocean environment with the sound speed field $C(s)$ and the current field $\mathbf{v}(s)$. The travel time of an acoustic pulse can be expressed by

$$t = \int_{\Gamma} \frac{ds}{C(s) + \mathbf{v}(s) \cdot \mathbf{r}(s)}, \tag{2.5}$$

where Γ denotes the ray path and $\mathbf{r}(s)$ is the tangent vector along the ray path at the position s. The sum of the $C(s)$ and $\mathbf{v}(s) \cdot \mathbf{r}(s)$ can be viewed as the effective sound speed at the position s. The travel time is the integral of the inverse of the effective sound speed along the ray path. When Stations 1 and 2 are stationary, the travel time of the pulse traversed from Station 1 to Station 2 can be expressed as

$$t_{12} = \int_{\Gamma_{12}} \frac{ds}{C(s) + \mathbf{v}(s) \cdot \mathbf{r}_{12}(s)}. \tag{2.6}$$

To consider the effect of the sound speed perturbation on the travel time, the sound speed in Equation (2.6) is linearized by

$$C(s) = C(s, -) + \Delta C(s), \tag{2.7}$$

where $C(s, -)$ denotes the known reference of the sound speed field and $\Delta C(s)$ denotes the perturbation of the sound speed field. The travel-time perturbation is

$$t_{12} - t(-) = \int_{\Gamma_{12}} \frac{ds}{C(s) + \mathbf{v}(s) \cdot \mathbf{r}_{12}(s)} - \int_{\Gamma_{(-)}} \frac{ds}{C(s, -)}. \tag{2.8}$$

10.6342/NTU201603287

For the experiment in this study, the sound speed perturbation $\Delta C(s)$ (less than 5 $\mathrm{m\,s^{-1}}$) and the current velocity $\mathbf{v}(s)$ (less than 1 $\mathrm{m\,s^{-1}}$) are much smaller than the reference sound speed $C(s,-)$ (about 1540 $\mathrm{m\,s^{-1}}$). The travel-time perturbation is approximated by

$$t_{12} - t(-) = \int_{\Gamma_{(-)}} \frac{\Delta C(s) + \mathbf{v}(s) \cdot \mathbf{r}_{12}(s,-)}{C^(s,-)}\, ds, \tag{2.9}$$

where $\Gamma_{12} \approx \Gamma_{(-)}$. The travel-time perturbation of the oppositely traveling pulse can be expressed in a similar manner:

$$t_{21} - t(-) = \int_{\Gamma_{(-)}} \frac{\Delta C(s) - \mathbf{v}(s) \cdot \mathbf{r}_{12}(s,-)}{C^(s,-)}\, ds. \tag{2.10}$$

Note that the sign of $\mathbf{v}(s) \cdot \mathbf{r}_{12}(s,-)$ in Equation (2.10) is reversed using the relation $\mathbf{r}_{12}(s) = -\mathbf{r}_{21}(s)$. Thus, the DTT $\Delta t_{12} = t_{12} - t_{21}$ is

$$\Delta t_{12} = -2 \int_{\Gamma_{(-)}} \frac{\mathbf{v}(s) \cdot \mathbf{r}_{12}(s,-)}{C^2(s,-)}\, ds. \tag{2.11}$$

In the presence of the transceiver motion, an additional term should be added to Equation (2.11):

$$\Delta t_{12} = -2 \int_{\Gamma_{(-)}} \frac{\mathbf{v}(s) \cdot \mathbf{r}_{12}(s,-)}{C^2(s,-)}\, ds + \frac{R}{c^2}(u_1 + u_2), \tag{2.12}$$

where the second term on the right-hand side of Equation (2.12), $\frac{R}{c^2}(u_1 + u_2)$, represents the effect of the instrument motions on the DTT. If u_1 and u_2 are known, the DTT can provide the measure for the path integral of the projected current velocity $\mathbf{v}(s) \cdot \mathbf{r}_{12}(s,-)$ on the ray $\Gamma_{(-)}$.

One may concern with the trajectory of the ray Γ in order to interpret the estimated path-averaged current velocity. Section 5.1 will present the eigenray simulations for the interpretation of estimated currents.

2.1.1 Limitation on Sensing the Divergence of the Currents

The acoustic mapping in this study can not sense the divergence of the currents inside the region surrounded by the deployed stations [20]. Using the Helmholtz's theorem, a two-dimensional current field $\mathbf{v}(x,y)$ can be decomposed as follows:

$$\mathbf{v}(x,y) = \nabla \mathbf{\Phi}(x,y) + \nabla \times \mathbf{\Psi}(x,y), \tag{2.13}$$

where $\nabla \mathbf{\Phi}(x,y)$ and $\nabla \times \mathbf{\Psi}(x,y)$ are referred to as the irrotational and the solenoidal parts, respectively. Norton [20] proved that the line integral of the irrotational part

10.6342/NTU201603287

of the currents over the path between the endpoints at the boundary of the region is zero. Therefore, the irrotational part of the currents can not be sensed by the line-integral measurements from the stations deployed outside the region.

The inability of sensing the irrotational part of the currents is not critical in this study. For the horizontal mapping of the ocean circulation, the irrotational part of the currents exists only when there is a divergence in the currents, implying the existence of the vertical currents, such as upwelling or downwelling. Since the vertical currents in the experiment site are small, the irrotational part of the currents in Equation (2.13) is omitted.

2.2 Methods for Current Estimation

2.2.1 Temporal Evolution

Assuming a uniform current velocity in the horizontal plane $\mathbf{v} = [v_{x,a}, v_{y,a}]^{\mathrm{T}}$, the equation for estimating the current velocity $\mathbf{v}$ is rewritten as follows:

$$\Delta\tilde{t}_{ij} = \Delta t_{ij} - \frac{R}{c^2}(u_i + u_j) = -\frac{2R}{c^2}\mathbf{v} \cdot \mathbf{r}_{ij} \tag{2.14}$$

where $\mathbf{r}_{ij}$ is the unit vector along the path from stations i to j, and $\Delta\tilde{t}_{ij}$ denotes the DTT for the reciprocal transmission between stations i and j after removing the influence of the velocities of the transceivers, u_i and u_j.

Assuming R, c, u_i and u_j are known, $\Delta\tilde{t}_{ij}$ can provide the measures for the current velocity along the direction $\mathbf{r}_{ij}$.

Combining the data from the acoustic transmission of N different station pairs (different $\mathbf{r}_{ij}$'s), the relationship between the discrete set of the DTT measurements and the current velocity can be represented by a matrix form

$$\mathbf{d} = \mathbf{G}\mathbf{v} + \mathbf{n}, \tag{2.15}$$

where $\mathbf{d}$ is a data vector containing N $\Delta\tilde{t}_{ij}$ measurements, and $\mathbf{G}$ is a $N \times 2$ matrix, referred to as the observation matrix. The kth row in $\mathbf{G}$ is the unit vector of the ray path for the kth DTT in $\mathbf{d}$. The vector $\mathbf{n}$ represents the measurement noise. For example, considering three pairs of the reciprocal transmission from Stations 1–3,

10.6342/NTU201603287

$\mathbf{d}$, $\mathbf{G}$, $\mathbf{v}$, and $\mathbf{n}$ can be written as:

$$\mathbf{d} = \begin{bmatrix} \Delta\tilde{t}_{12} \\ \Delta\tilde{t}_{23} \\ \Delta\tilde{t}_{13} \end{bmatrix}, \tag{2.16}$$

$$\mathbf{G} = \begin{bmatrix} r_{12,x} & r_{12,y} \\ r_{23,x} & r_{23,y} \\ r_{13,x} & r_{13,y} \end{bmatrix}, \tag{2.17}$$

$$\mathbf{v} = \begin{bmatrix} v_{\mathrm{x}} \\ v_{\mathrm{y}} \end{bmatrix}, \tag{2.18}$$

$$\text{and } \mathbf{n} = \begin{bmatrix} n_{12} \\ n_{23} \\ n_{13} \end{bmatrix}. \tag{2.19}$$

When there exist at least two DTT measurements, $\mathbf{v}$ can be estimated using the least squares method. The least squares method finds $\mathbf{v}$ such that the norm of $(\mathbf{d} - \mathbf{G}\mathbf{v})$ reaches the minimum. The estimated current vector can be found:

$$\bar{\mathbf{v}} = (\mathbf{G}^{\mathrm{T}}\mathbf{G})^{-1}\mathbf{G}^{\mathrm{T}}\mathbf{d}. \tag{2.20}$$

2.2.2 Spatial Distribution

For the spatial distribution of the current field, the method proposed by Huang *et al.* [10] is applied to reconstruct the current field. The algorithm of the current reconstruction is summarized in Figure 2.3.

The domain of the estimation is divided by the triangles, which are the basic units formed by three nearby stations. The DTT measurements along the three ray paths can be used to estimate the current within the triangle. One example of the triangle is formed with Stations 1–3 as shown in Figure 2.3(b). This triangle is further divided by four sub-triangles. The current vectors at the centroids of the three corner sub-triangles are explicitly calculated with the assumption that the spatial variation of the current is low within the triangle. The current vector at the centroid of the sub-triangle a, $\bar{\mathbf{v}}_a = [\bar{v}_{x,a}, \bar{v}_{y,a}]$, can be calculated by:

$$\bar{v}_{x,a} = \frac{c^2(s_{13}\sin\theta_{13}\Delta t_{12} - s_{12}\sin\theta_{12}\Delta t_{13})}{s_{12}s_{13}\sin(\theta_{12} - \theta_{13})} \tag{2.21}$$

$$\bar{v}_{y,a} = \frac{c^2(s_{12}\cos\theta_{12}\Delta t_{13} - s_{13}\cos\theta_{13}\Delta t_{12})}{s_{12}s_{13}\sin(\theta_{12} - \theta_{13})} \tag{2.22}$$

The current vectors at the centroids of the other sub-triangles b and c can also be calculated using a similar manner. Once $\mathbf{v}_a$, $\mathbf{v}_b$ and $\mathbf{v}_c$ are estimated, the current

10.6342/NTU201603287

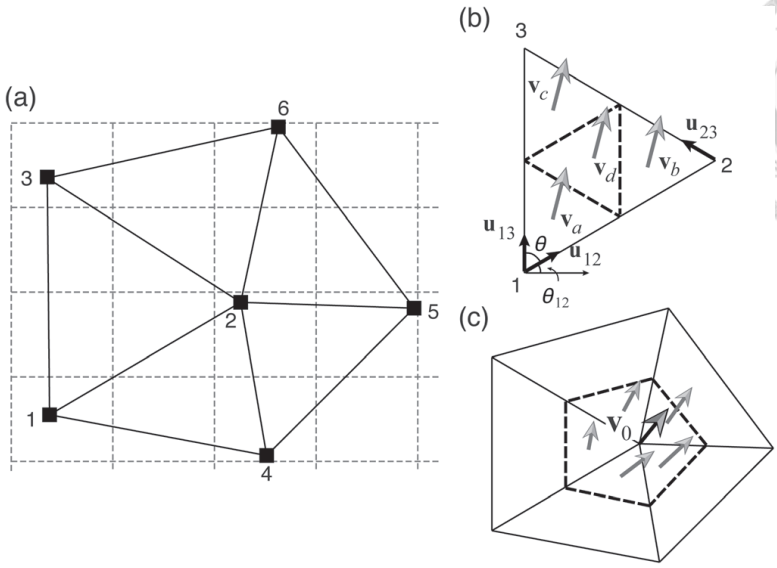

Figure 2.3: Algorithm of the current reconstruction proposed by Huang *et al.* [10].

vector at the centroid of the sub-triangle d, $\mathbf{v}_d$, can be calculated by:

$$\bar{\mathbf{v}}_d = \frac{\bar{\mathbf{v}}_a + \bar{\mathbf{v}}_b + \bar{\mathbf{v}}_c}{3} \tag{2.23}$$

and the current vector at the station where several triangles intersect [Figure 2.3(c)] is given by:

$$\bar{\mathbf{v}}_0 = \frac{1}{P}\sum_{i=1}^{P} \bar{\mathbf{v}}_i \tag{2.24}$$

where the set of $\bar{\mathbf{v}}_i$'s is the estimated current vectors in the neighboring P sub-triangles. Finally, the current field is computed using the triangle-based linear interpolation with the determined vectors ($\bar{\mathbf{v}}_a$, $\bar{\mathbf{v}}_b$, $\bar{\mathbf{v}}_c$, $\bar{\mathbf{v}}_d$, and $\bar{\mathbf{v}}_0$).

2.3 Basic Signal-Processing Techniques

2.3.1 Pulse Compression

Pulse compression is a signal-processing technique that is widely used in the radar system. The technique can increase the time resolution and the SNR of a received signal. To apply pulse compression, the transmitter transmits a signal, and the received signal is then matched filtered with the replica of the transmitted signal. The common choices for the transmitted signals are the *m*-sequence coded phase modulation wave and linear frequency modulation (LFM) wave.

This section uses a simplified example to explain the technique. Consider a source and a receiver in the channel. The channel impulse response is expressed by

10.6342/NTU201603287

$h(t) = a_1\delta(t - t_1) + a_2\delta(t - t_2)$ [Figure 2.4(b)], where $a_1 = 0.8$, $a_2 = 0.2$, $t_1 = 1.20$, and $t_2 = 1.23$. The source transmits a signal $s(t)$, which is a binary wave coded by a 10th-order m sequence (1023 bits, the same signal applied in the field experiment) [Figure 2.4(a)]. The transmitted signal $s(t)$ is then amplitude-attenuated and time-delayed by the channel. The received signal (at the receiver) can be expressed by $r(t) = a_1 s(t - t_1) + a_2 s(t - t_2) + n(t)$ [Figure 2.4(c)], where $n(t)$ denotes the white Gaussian noise. The average power of $n(t)$ is four times of $s(t)$. Thus, the transmitted signal is buried in the noise. Finally, the received signal $r(t)$ is matched filtered with the replica of transmitted signal $s(t)$ as follows:

$$y(\tau) = \int r(t)s(t - \tau)dt \tag{2.25}$$

The output of the matched filtering $y(\tau)$ consists of two delayed pulses at the t_1 and t_2, with the amplitudes of a_1 and a_2, respectively [Figure 2.4(d)]. It can be seen that these two arrivals can be identified separately even though the time separation between two arrivals is 0.03 s, which is much smaller than the length of the transmitted signal (about 0.2 s). One can also increase the amplitudes of the resolved pulses with longer m-sequences.

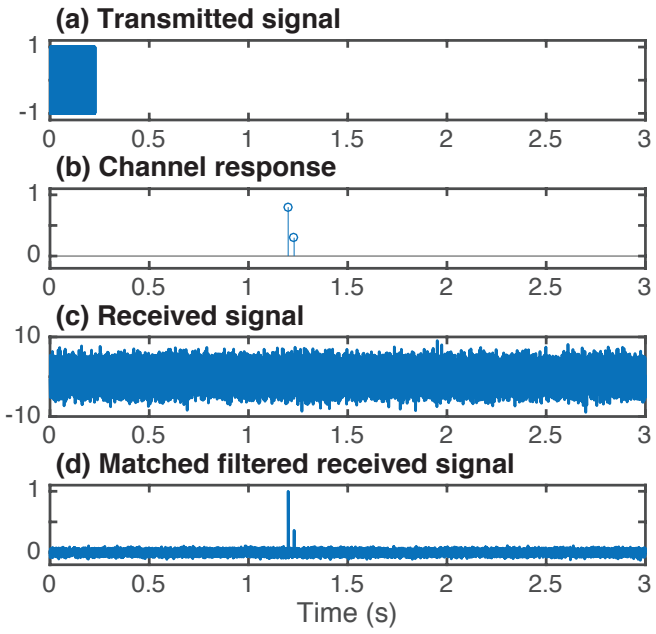

Figure 2.4: (a) The transmitted signal. (b) The channel impulse response. (c) The received signal. (d) The matched filtered received signal.

The advantage of the pulse compression is that one can obtain the channel pulse response without actually transmitting pulses. Transmitting a pulse with an enough

10.6342/NTU201603287

signal energy requires a high instantaneous power of the acoustic transducer, which is usually a challenging task. Using this technique, one can increase the SNR of the received signal with longer transmitted signals and improve the time resolution with a broader bandwidth of the transmitted signal.

2.3.2 Maximum-length Sequence

The maximum-length sequence (m-sequence) is a type of the pseudo-random binary sequences. Each m-sequence is a sequence of binary bits, either "0" or "1", with the occurrence of the 0 bits and 1 bits in a pseudo-random fashion. The number of bits in the m-sequence depends on the order of the m-sequence. The nth-order m-sequence has $2^n - 1$ bits. One important property of the m-sequence is that the autocorrelation function of the m-sequence has a sharp peak at the lag of zero and is close to zero at other lags. The cross-correlation between two differently coded m-sequences is small. Thus, one can distinguish one m-sequence from another.

The m-sequence coded signal is an ideal signal for the pulse compression processing because of its pulse-like autocorrelation function. The received signal of the m-sequence coded signal can be "compressed" by cross-correlating the reception with the replica of the transmitted signal. Figure 2.5(a) illustrates a typical nth-order m-sequence. The 0 bits in the m-sequence are mapped to -1. The autocorrelation function of the sequence [Figure 2.5(b)] exhibits a sharp pulse at the lag of zero with the maximum height, which is $2^n - 1$ times higher than the ones of other lags.

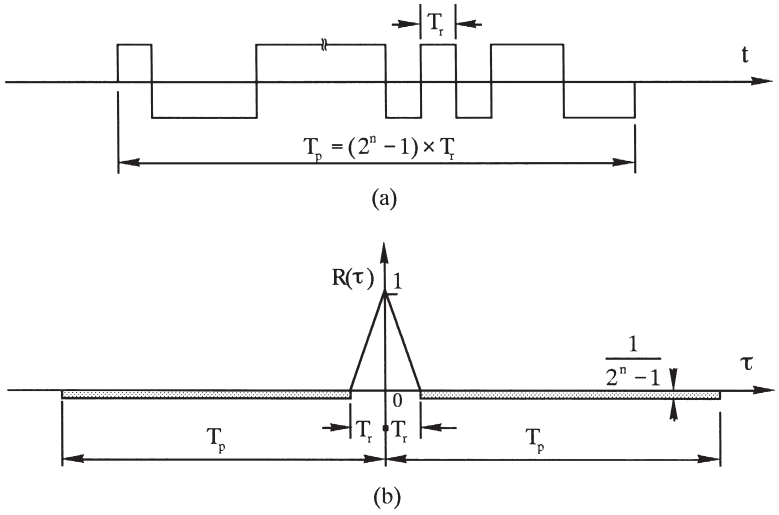

Figure 2.5: (a) A close look of a period of the m-sequence. (b) The autocorrelation function of the one-period m-sequence [38].

10.6342/NTU201603287

2.3.3 Binary Phase Shift Keying Modulation

Modulation is a process that embeds the message into the carrier signals. Three major modulation schemes are amplitude, frequency and phase modulation, which modulate the amplitude, frequency, and phase of the carrier signal according to the message. For the binary phase shift keying (BPSK), the phase of the carrier signal is modulated according to the bits in the message.

Figure 2.6 shows an example of BPSK modulation with a 5-bit message and a carrier signal with the frequency of f_c. The phase of the carrier signal [$c(t) = \sin(2\pi f_c t)$ in Figure 2.6(b)] is shifted according to the bits in the message: the phase of the carrier signal is reversed in response to the "0" bits. The modulated signal is shown in Figure 2.6(c).

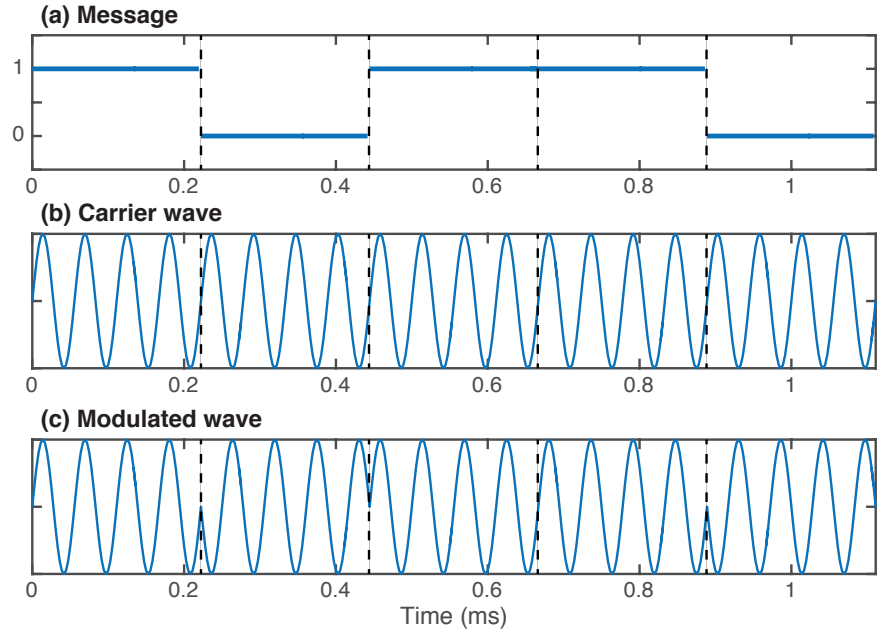

Figure 2.6: (a) The 5-bit message. (b) The carrier signal. (c) The modulated signal.

2.3.4 Cross-correlation Function

The cross-correlation provides the quantity for the similarity between two waveforms. The cross-correlation function between the two discrete-time waveforms, $x[n]$ and $y[n]$, is defined as

$$c_{xy}[m] = \sum_{n=-\infty}^{\infty} x[n+m]y^*[n]. \tag{2.26}$$

The cross-correlation $c_{xy}[m]$ is a function of lag m, and the quantity $c_{xy}[m]$ is the dot product between $y[n]$ and $x[n]$ shifted by m samples. High cross-correlation is

10.6342/NTU201603287

present when the waveforms $y[n]$ and $x[n]$ have a similar pattern.

The cross-correlation defined in Equation (2.26) depends on not only the similarity between input waveforms but also the magnitudes of the waveform, e.g., the cross-correlation is scaled when either input waveform is scaled. To remove the effects of the waveform magnitude on the cross-correlation, we normalize the cross-correlation by the norms of the input series:

$$c'_{xy}[m] = \frac{c_{xy}[m]}{\sqrt{c_{xx}[0]c_{yy}[0]}}. \tag{2.27}$$

The normalized cross-correlation function $c'_{xy}[m]$ is not affected by the magnitudes of the input series, and its range is limited: $-1 \leq c'_{xy}[m] \leq 1$. Thus, the autocorrelation of a series is unity at lag zero. Having the unified range of the correlation, the quantities of the cross-correlation are now comparable, i.e., the quantities of the cross-correlation function $c'_{x_iy_i}$ is comparable with that of the another function $c'_{x_jy_j}$.

When the reciprocal arrivals exhibit a similar pattern except for the slight time difference induced by the current, the time difference may be estimated by the lag time of the maximum cross-correlation value.

2.4 Doppler Signal Processing

The Doppler effect arises in the underwater acoustic channel when the transceivers have relative motion during the signal transmission or reception. Consider a transmitter and a receiver in an infinite medium (as shown in Figure 2.7) and both instruments are stationary ($|\mathbf{u}_\mathrm{r}| = 0$). The transmitter transmits an acoustic signal $s(t)$ at $t = 0$. Omitting the attenuation of the acoustic signal, the receiver receives the signal $r(t) = s(t-\tau)$, which is the delayed replica of the transmitted signal. The propagation delay τ is given by a constant R/c, where R denotes the propagation distance and c is the sound speed.

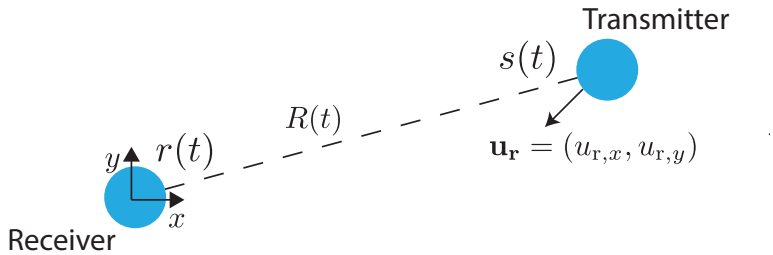

Figure 2.7: Travel-time measurement with the relative motion of transceivers. $s(t)$ and $r(t)$ denote the transmitted and received signals, respectively.

10.6342/NTU201603287

In this study, the mobile transceiver was towed with a constant speed along segments of straight lines. To investigate the Doppler effect on the signal, we consider the presence of the relative motion between the transceivers: the transmitter is moving with a constant velocity $\mathbf{u}_{\mathrm{r}} = (u_{\mathrm{r},x}, u_{\mathrm{r},y})$ relative to the receiver in the horizontal plane. Let the origin at the receiver, the time-variable position of the transmitter is expressed by $\mathbf{R}(t) = (R_x - u_{\mathrm{r},x}t,\ R_y - u_{\mathrm{r},y}t)$, where R_x and R_y denote the distance between the instruments at the time $t = 0$ projected on the x- and y- axes, respectively. To simplify the derivation, a unit vector is defined along the transmitter-receiver axis at $t = 0$: $\mathbf{r} = (R_x/R(0), R_y/R(0))$. The distance between the instruments as a function of time can be written as

$$R(t) = |\mathbf{R}(t)| = \sqrt{(R_x - u_{\mathrm{r},x}t)^2 + (R_y - u_{\mathrm{r},y}t)^2}. \tag{2.28}$$

The travel time is a function of time and is expressed by

$$\tau(t) = \frac{R(t)}{c}. \tag{2.29}$$

Also, the received signal $r(t)$ can be written as

$$r(t) = s[t - \tau(t)], \tag{2.30}$$

i.e., the received signal at the time t (from the receiver) was transmitted at the time $t - \tau(t)$ (at the transmitter),

Next, we expand $\tau(t)$ in a Taylor series about the reference time $t = 0$:

$$\tau(t) = \tau(0) + \tau_t(0)t + \tau_{tt}(0)\frac{t^2}{2} + \text{Higher order terms}, \tag{2.31}$$

where the first term $\tau(0)$, the second term $\tau_t(0)$, and the third term $\tau_{tt}(0)$ in Equation (2.31) are

$$\tau(0) = \frac{\sqrt{{R_x}^2 + {R_y}^2}}{c} = \frac{R(0)}{c}, \tag{2.32}$$

$$\tau_t(0) = -\frac{R_x\, u_x + R_y\, u_y}{c\sqrt{{R_x}^2 + {R_y}^2}} = -\frac{\mathbf{u}_{\mathrm{r}} \cdot \mathbf{r}}{c}, \tag{2.33}$$

$$\text{and } \tau_{tt}(0) = \frac{\frac{{u_x}^2 + {u_y}^2}{\sqrt{{R_x}^2 + {R_y}^2}} - \frac{(R_x\, u_x + R_y\, u_y)^2}{\left({R_y}^2 + {R_y}^2\right)^{\frac{3}{2}}}}{c} = \frac{\mathbf{u}_{\mathrm{r}} \cdot \mathbf{u}_{\mathrm{r}} - (\mathbf{u}_{\mathrm{r}} \cdot \mathbf{r})^2}{c\, R(0)}. \tag{2.34}$$

Note that it should be sufficient to represent $\tau(t)$ in Equation (2.31) with the first two terms since the third term is small in this study. To show the influence of $\tau_{tt}(0)$ on Equation (2.31), we apply the scale analysis to study the ratio $|\tau_{tt}(0)/\tau_t(0)|$:

$$\left|\frac{\tau_{tt}(0)}{\tau_t(0)}\right| = \frac{\left|\mathbf{u}_{\mathrm{r}} \cdot \mathbf{u}_{\mathrm{r}} - (\mathbf{u}_{\mathrm{r}} \cdot \mathbf{r})^2\right|}{R(0)\ |\mathbf{u}_{\mathrm{r}} \cdot \mathbf{r}|} \approx \frac{|\mathbf{u}_{\mathrm{r}}|}{R(0)}. \tag{2.35}$$

10.6342/NTU201603287

The ratio is about 10^{-3} based on the typical values of $R(0) = 1$ km and $|\mathbf{u}_\mathrm{r}| = 1.5\,\mathrm{m\,s^{-1}}$. Also, the signal duration was about 0.2 s. Due to the short duration of the signal and the small ratio of $|\tau_{tt}(0)/\tau_t(0)|$, the third term is negligible in this study. It is therefore sufficient to represent $\tau(t)$ with the first two terms:

$$\tau(t) = \frac{R(0)}{c} - \frac{u_\mathrm{r}}{c}t, \tag{2.36}$$

where $u_\mathrm{r} = \mathbf{u}_\mathrm{r} \cdot \mathbf{r}$ is the relative velocity along the radial direction.

Substituting the time-variable travel time $\tau(t)$ in Equations (2.36) into (2.30), the received signal becomes

$$r(t) = s(\alpha t - \tau_0), \tag{2.37}$$

where $\alpha = 1 + u_\mathrm{r}/c$ and $\tau_0 = R(0)/c$.

The Doppler effect essentially compresses or expands the transmitted signal corresponding to the Doppler scaling factor α. The signal used in the experiment is a wideband signal since the ratio of bandwidth (4.5 kHz) to the carrier frequency (18 kHz) is larger than 0.1. The commonly used narrow-band approximation, which models the Doppler effect by a shift of the carrier frequency, is invalid for the wideband signals used in this experiment.

In addition to the effects on the received waveform, the Doppler-processing technique is also discussed. The first step of the processing is to estimate the Doppler factor α of the received signal. The Doppler factor can be estimated based on the wideband delay-Doppler ambiguity function:

$$\chi(\tau, \alpha) = \int r(t)s(\alpha t - \tau)dt, \tag{2.38}$$

where the received signal is correlated with different Doppler shifted replicas of the transmitted signal $s(t)$. Note that both $s(t)$ and $r(t)$ in Equation (2.38) are real-valued passband signals.

For the baseband signals, Equation (2.38) should be modified to include the shift of the carrier frequency:

$$\chi(\tau, \alpha) = \int \tilde{r}^*(t)\tilde{s}(\alpha t - \tau)\exp(j2\pi(\alpha - 1)f_\mathrm{c}t)dt, \tag{2.39}$$

where $\tilde{s}(t)$ denotes the baseband transmitted signal and $\tilde{r}^*(t)$ the complex conjugate of the baseband received signal. The last term in the integral, $\exp(j2\pi(\alpha - 1)f_\mathrm{c}t)$, compensates for the Doppler shift of the carrier frequency.

The characteristics of the ambiguity function vary for different types of the signal. Figure 2.8 shows the ambiguity functions of (a) the phase modulated signal coded by the m-sequence applied in the field experiment (see Table 3.2 for details),

10.6342/NTU201603287

(b) the linear frequency modulation (LFM) signal which has the same time duration and bandwidth as the m-sequence coded signal, (c) the short-tone ping of 18 cycles, and (d) the long-tone ping of 7195 cycles (the same carrier frequency as employed in the experiment). It can be seen that the m-sequence coded signal exhibits high resolutions in both delay and Doppler axes. For the LFM signal both delay and Doppler variables are coupled. The CW signals could not achieve high resolutions in both delay and Doppler simultaneously: The long-tone ping has high Doppler resolution but has poor delay resolution. In contrast, the short-tone ping has high resolution in delay but provides poor Doppler estimate. Also, note that the short-tone ping may require high transmission power to convey a sufficient signal energy within the short period.

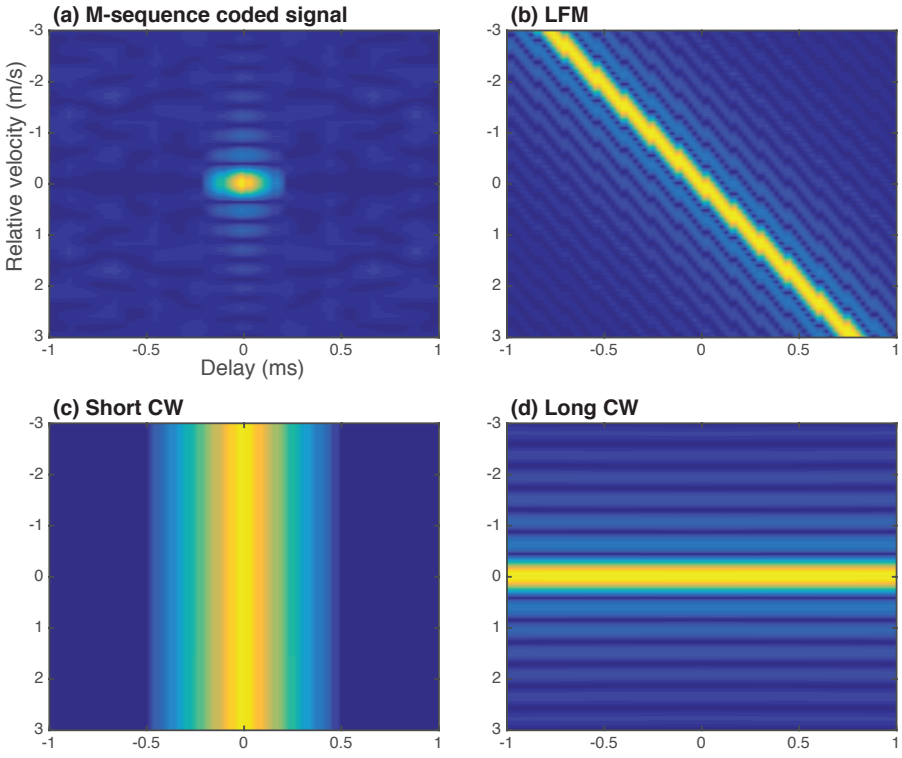

Figure 2.8: Delay-Doppler ambiguity functions for various signals: (a) phase-modulated signal coded by the m-sequence, (b) the LFM signal, (c) the short-tone ping, and (d) the long-tone ping.

The Doppler factor $\hat{\alpha}_0$ and the travel time $\hat{\tau}_0$ of the received signal can be estimated via

$$(\hat{\tau}_0, \hat{\alpha}_0) = \arg\max_{\tau,\alpha} |\chi(\tau, \alpha)| . \tag{2.40}$$

When the relative motion does not exist, the arrival pattern (pulse response) can be obtained by matched filtering the received signal with the replica of the

10.6342/NTU201603287

transmitted signal [Equation (2.25)]. Whereas when the signal is Doppler-shifted, the matched filter should be modified according to the Doppler shift as follows:

$$y(\tau) = \int r(t)s(\hat{\alpha}_0 t - \tau)dt, \tag{2.41}$$

which is equivalent to

$$y(\tau) = |\chi(\tau, \hat{\alpha}_0)|. \tag{2.42}$$

The arrival pattern can be obtained by substituting the estimated Doppler factor $\hat{\alpha}_0$ into the ambiguity function. Also, the relative velocity u_{r} can then be estimated from $\hat{\alpha}_0$:

$$u_{\mathrm{r}} = (\hat{\alpha}_0 - 1)\, c. \tag{2.43}$$

Note that u_{r} is positive when the transmitter and the receiver move closer, in which $\hat{\alpha}_0$ is greater than unity and the transmitted signal is time compressed. In a real underwater acoustic channel, the received signals are usually composed of multipath arrivals, and the Doppler factors may differ for the arrivals.

2.5 Summary

This chapter reviewed the principle of the acoustic mapping for the ocean currents and the relevant theories for the following chapters. The main concept is that the differential travel time (DTT) from the reciprocal acoustic transmission provides the measures of the integrated current velocity along the ray path. The current can be reconstructed from the DTT measurements. The currents estimation depends on the precise acoustic travel-time measurements, which can be achieved by the signal-processing techniques. The phase-modulated signal coded by the *m*-sequence is used as the transmitted signal because the autocorrelation of an m-sequence approaches unit impulse function. The different acoustic arrivals can be individually resolved with the adequate SNR and high time resolution by the matched filter. In the presence of the relative motion between transceivers, one may compensate the Doppler distortion of the received signals using the wideband delay-Doppler ambiguity function. The cross-correlation function was computed for the reciprocal arrival patterns. The lag times corresponding to the higher cross-correlation values were used to determine the DTT.

10.6342/NTU201603287

Chapter 3

Field Experiment

3.1 Description of the Experiment

The field experiment was conducted at Sizhiwan Marine Test Field (MTF) with the R/V Ocean Researcher III. The experiment time was from August 30 to September 2, 2015. Four moored stations (M1–M4) were deployed, and one mobile station (M5) was towed by the research vessel.

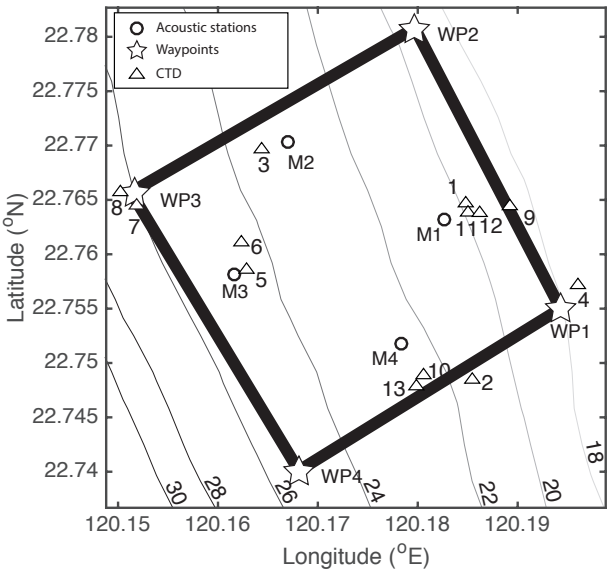

Figure 3.1: Bathymetry of the experimental site and the instruction positions.

Figure 3.1 shows the bathymetry of the experiment site, the positions of the moored stations (indicated by the circle), the tow track (black line) and the waypoints of the tow track (star symbols). The experiment site is about 20 km from the port of Kaohsiung and is 6 km offshore from the coast. The water depth varies from 20 to 26 m with the isobaths parallel to the coastline. The area is dominated

10.6342/NTU201603287

by the semi-diurnal tide. The principal axis of the tidal currents is parallel to the isobath [35].

The four moored stations were deployed at the corner of a quadrilateral. To avoid the overlap of signals coming from different stations, the side lengths of the quadrilateral were designed purposely different and varied from 1.4 km to 1.8 km. The mobile station was towed by the research vessel along the square path with the speed of about 1.5 $\mathrm{m\,s^{-1}}$. The side length of the tow track is about 3.2 km. The GPS positions of the moored stations and the waypoints of the tow track are listed in Table 3.1. With the mobile station, the position of the station varied with time, and the acoustic rays between the moored and towed stations transverse through the ocean at various angles. The distance between the moored and the towed stations varied from 0.5 km to 3.5 km.

In addition to the travel-time measurements, the hydrographic data were collected. 13 conductivity, temperature and depth (CTD) casts were conducted to derive the sound speed profiles (SSPs). The SSPs are to study the propagation path of the acoustic signals in the underwater channel. The shipboard acoustic Doppler current profiler (ADCP) on R/V ORIII measured the current velocity beneath the vessel. The shipboard-ADCP provides the direct measurement of the ocean currents at the experiment site.

Table 3.1: Location of the moored stations

Name	Longitude	Latitude
M1	120°11.358' E,	22°45.816' N
M2	120°10.910' E,	22°44.767' N
M3	120°09.770' E,	22°45.176' N
M4	120°10.224' E,	22°46.220' N
WP1	120°08.859' E,	22°45.816' N
WP2	120°11.248' E,	22°47.062' N
WP3	120°12.273' E,	22°44.890' N
WP4	120°09.884' E,	22°43.929' N

The operation periods of the instruments are listed in Figure 3.2. Usually, there were at least three moored stations operating. M1, M2, and M4 were deployed during the entire experiment except for the temporary recovering of M1 and M4. Unfortunately, M1 did not receive signals properly after 5 am of August 31. M3 was deployed on the last three days of the experiment. The towed station, M5, was operated in the daytime on August 30, 31 and September 2.

10.6342/NTU201603287

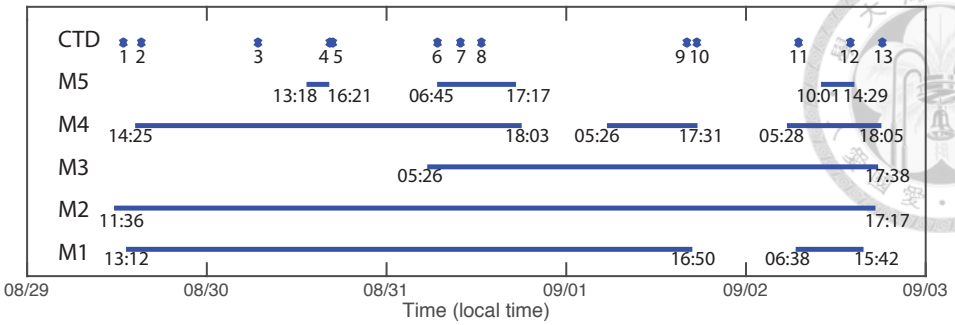

Figure 3.2: Operation period of the instruments.

Figure 3.3 illustrates the deployment of the moored stations. Each moored station was composed of a surface expression (the orange buoy) and the acoustic transceiver (the gray device beneath the surface expression) with an underwater cable and a rope connecting both. A pressure sensor was attached near the transceiver to record the depth. The underwater cable was longer than the rope so that the tension only applied to the rope. Since the transceiver were not bottom-mounted, it could drift with ocean flow. A weight was installed at the end of the transceiver to reduce its motion. The surface buoy was connected to the concrete block (gray block in the lower left) lied fixedly on the sea floor with a rope. The pennant and the pickup float attached to the surface buoy provide assistance for the recovery of the instruments.

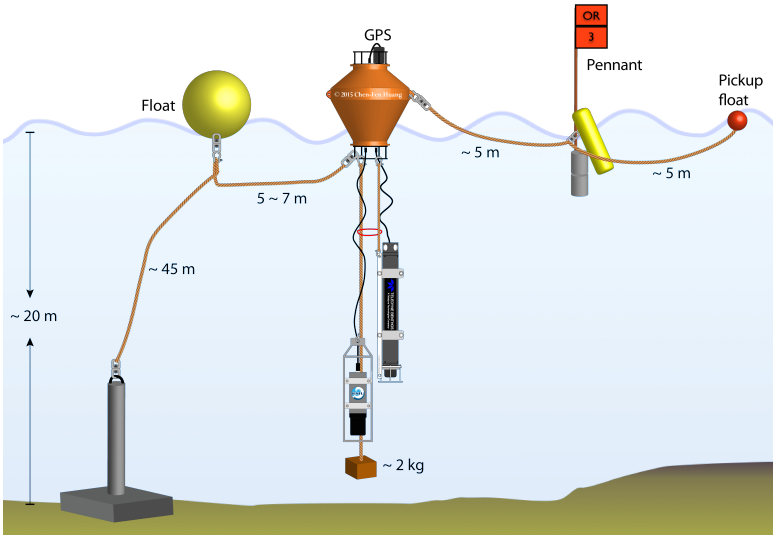

Figure 3.3: Configuration of tomographic mooring. Figure courtesy of Chen-Fen Huang

The depth of the transceiver was measured by the co-located pressure sen-

10.6342/NTU201603287

sor. Figure 3.4 shows the time series of the transceiver depth. The depth of the transceiver for the moored station changed slightly with time except when the current was strong. When the current is strong, the mooring was dragged horizontally by the current. Since the transceiver was at the end of the rope connecting to the surface buoy (Figure 3.3), the mooring rope had a high tilting angle. This high tilting angle resulted in a decrease of the transceiver depth. As for the mobile station (green line), the transceiver was at the depth of about 16 m on August 30. On August 31, the depth of the transceiver varied from 10 m to 14 m. On September 2, the tow depths were about 2 m.

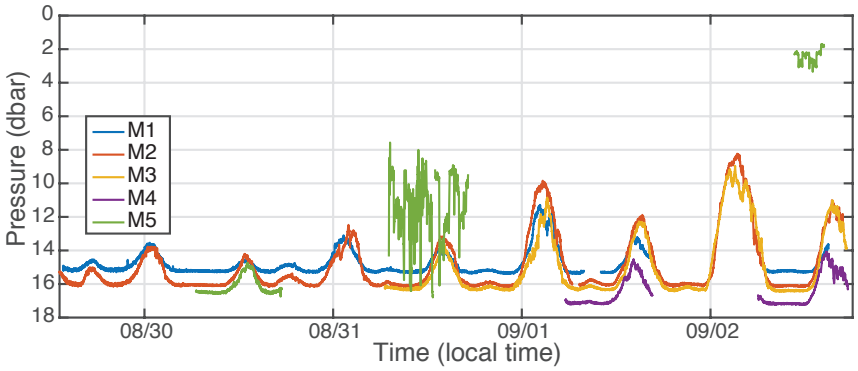

Figure 3.4: Time series of the transceiver depth measured by the pressure sensor.

3.2 Instruments for Acoustic Tranmission

There are only a few commercial instruments available for conducting precise travel-time measurements. This study uses the instruments designed by Naokazu Taniguchi and developed in Acoustical Oceanography Laboratory, National Taiwan University. Each instrument (station) is equipped with an acoustic transceiver and a surface unit. The station can transmit and receive the acoustic signals from the other remote stations with a high time precision. Figure 3.5 shows the photos of the system. There are two types of the surface unit: the orange buoy and the yellow box are surface units for the moored and mobile stations, respectively. The surface unit contains various components including a GPS receiver, the circuits, and batteries.

Figure 3.6 shows the components of an observation station. The major components are:

- **Transceiver:** Each station is equipped with a T235 model transducer from Neptune Sonar Ltd. The T235 transducer is broadband, horizontally omni-

10.6342/NTU201603287

directional [18]. The T235 transducers operate in the frequency band from 10 kHz to 25 kHz. The frequency responses of the transducer are shown in Figure 3.7. The transducer in this study operates at the center frequency of about 18 kHz with the bandwidth of about 4.5 kHz. Also, due to a high impedance of the transducer, the circuits interfacing the transducers, including the pre-amplifier and the transmit amplifier, were designed to match the impedance of the transducers.

- **Pre-amplifier:** The pre-amplifier is the receiving circuit for amplifying signals at the first stage. It is installed near the transducer and amplifies the weak electric signals from the transducer. The amplified signals then travel through an underwater cable (about 20 m long) to the signal conditioning circuits in the surface unit. To adpat the high impedance of the transducers, the pre-amplifiers were properly designed to extract the signals effectively from the transducer.

- **The GPS receiver**: Each station is equipped with a GPS receiver of LEA6T model from u-blox [29]. In addition to the position measurements, the GPS receiver provides accurate timing sources for the system. The time sources include two forms: the pulse per second (PPS) signal and 10 MHz clock signal. The PPS signal is an electric signal which has sharply rising (or falling) edges and repeats every second. The edge of the PPS signal is aligned to the seconds of Coordinated Universal Time (UTC) so that the networked stations could share a common time reference with an accuracy of 1 μs [29]. For travel-time measurements, the PPS signal is used to trigger time-critical tasks, e.g., the start of the acoustic transmission. The 10 MHz signal provides a stable, low jitter clock for the transmission and reception of the acoustic signals.

  The GPS antenna must be able to see the sky to acquire the signals from the satellites. For the moored station, the antenna is installed at the top of the buoy (above the sea surface). Whereas for the mobile station, the antenna is on the deck of the research vessel.

  The data obtained from the GPS receiver include the latitude, longitude, the time stamp, etc. These data are recorded on the SD memory card. Note that due to the current effect on the rope connecting the transceiver, the position of transceiver submerged 15 m below the water is different from the GPS position measured at the surface buoy. Thus, the position of the transceiver is known with uncertainty.

10.6342/NTU201603287

- **Programmable System-on-Chip**: The programmable system-on-chip (pSOC) from Cypress Semiconductor Corporation is the control center of the instruments [4]. The pSOC is responsible for the tasks including scheduling the transmission and reception of the acoustic signals, synchronizing the system time to the UTC, and the signal processing (demodulation, digitization and storing the received acoustic signals).

  The pSOC integrates many modules, including the analog to digital converters (ADC), digital filters, digital I/O buses and a programmable gain controller, into one integrated circuit (IC) chip. The manufacturer also provides the free development tools. The firmware operating on the pSOC was designed to avoid latencies of the time critical tasks, such as the transmission and reception of the acoustic signals.

- **Memory card**: The secure digital (SD) memory card is used to store the received acoustic signals organized by the FAT32 file system. The data files can be retrieved on the computers that support access to memory cards without specific software. For the reliability, it is recommended to use the memory cards from the credible manufacturers.

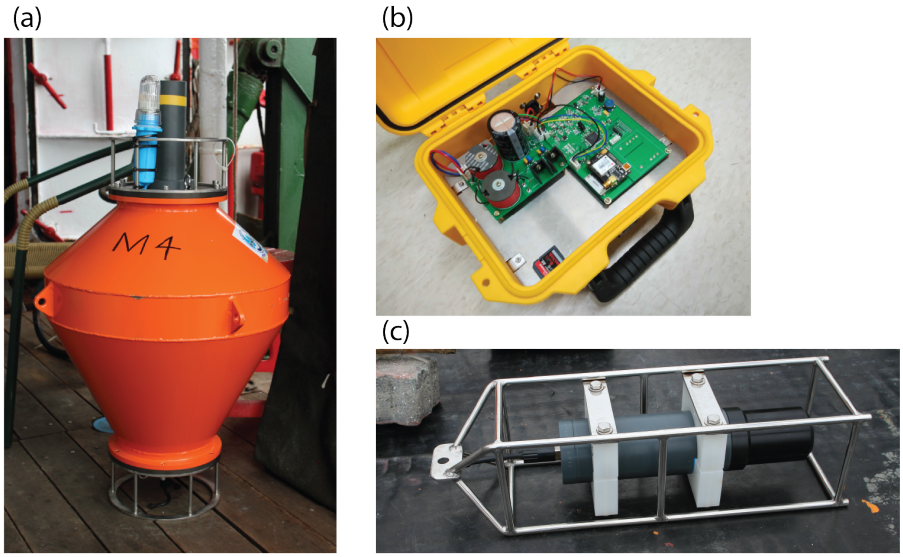

Figure 3.5: Photographs of the acoustic station. (a) The surface unit of the moored station. (b) The surface unit of the mobile station. (c) The transceiver and the pre-amplifier.

10.6342/NTU201603287

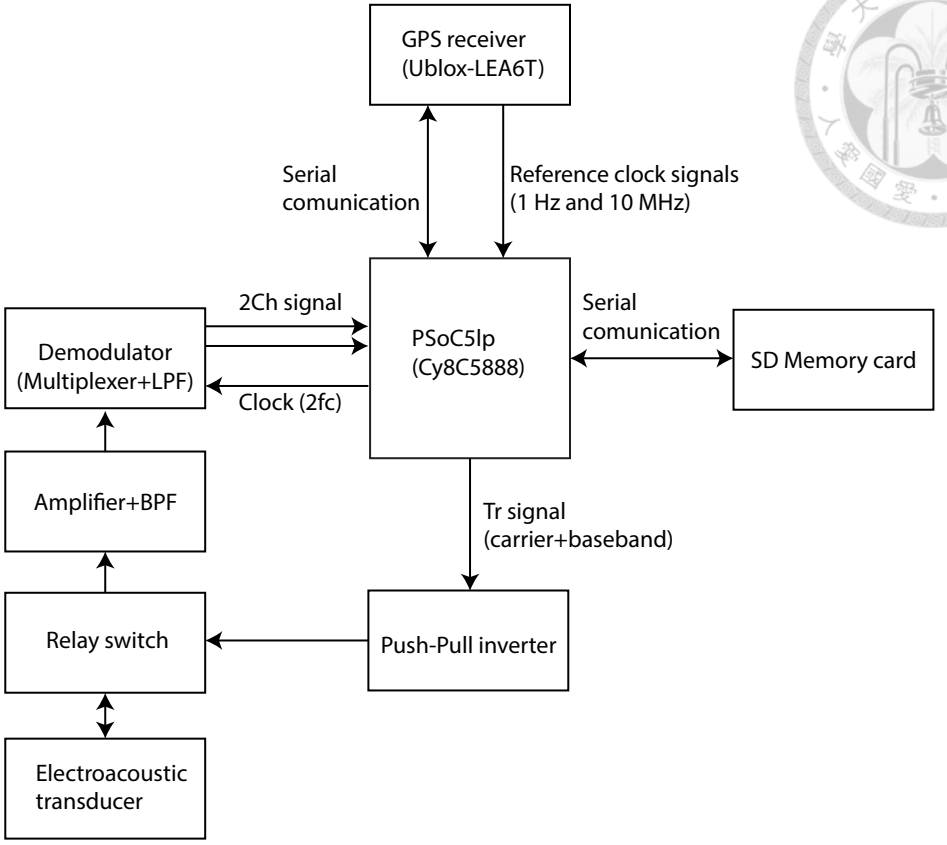

Figure 3.6: Block diagram of the acoustic station. [8]

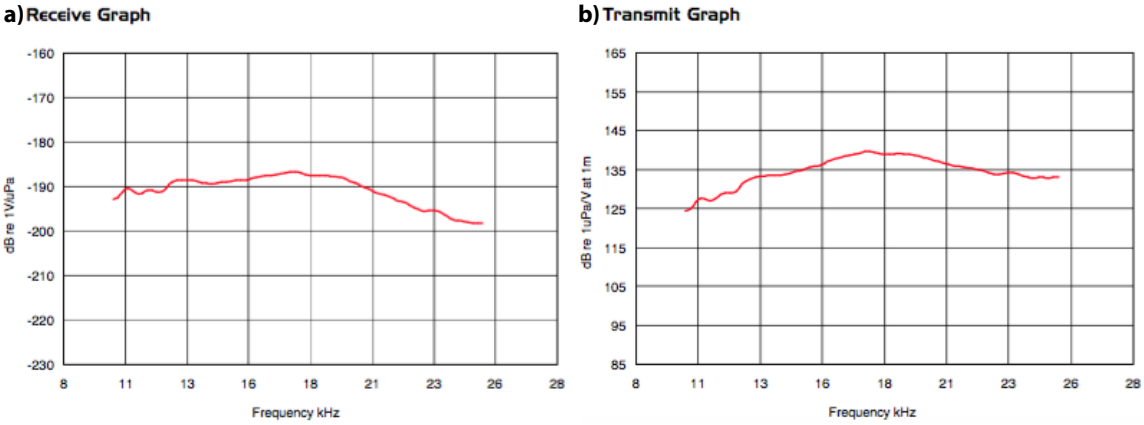

Figure 3.7: (a) Transmitting and (b) receiving responses of T235 model transceivers from Neptune Sonar Ltd [18].

Figure 3.8 shows the time line of each acoustic transmission for an acoustic station. First, the station transmits the acoustic signal with the time duration of about 0.2 s. All the networked stations simultaneously transmit the sequences.

10.6342/NTU201603287

Then, the station switches to the reception mode, recording the acoustic signals transmitted from other remote stations. The time window of the signal reception was set to about 3 s during the experiment. The time window should be wide enough to receive all the signals. The received signals, the transmission time, and the GPS position are stored on the memory card. Lastly, the station waits until the next transmission test. The transmission test was repeated every 30 s.

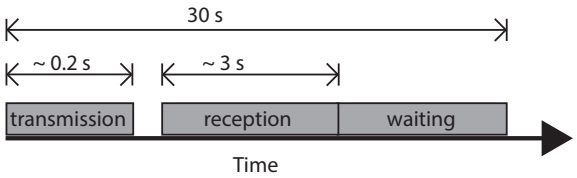

Figure 3.8: Time line of one acoustic transmission during the feasibility test in MTF.

Table 3.2: Configuration of the acoustic transmission.

Carrier frequency	17.986 kHz
Bandwidth	∼4.5 kHz
Number of cycles per bit	4
Number of bits in the *m*-sequence	1023
Bit length	0.22 ms
Signal duration	0.23 s
Transmission interval	30 s
Sampling frequency	35.9720 kHz
Number of bits in the ADC	12

The transmitted signal is the phase-encoded linear maximum shift-register sequence (*m*-sequence) with the carrier frequency of about 18 kHz (17.986 kHz). The *m*-sequence contains 1023 bits, and each bit is transmitted with four cycles of the carrier wave, resulting in the time resolution of 0.22 ms. The total length of a sequence is about 0.23 s. Each station transmits a differently coded *m*-sequence. Thus, one can identify the transmitted station in the received signals based on the code of the *m*-sequence.

The reception of the acoustic signals is also discussed here. As shown in Figure 3.6, the transducer measures the acoustic signals and converts the signals to the electric form. The electric signals are then amplified and filtered using a bandpass filter. The signals (passband signals) are then processed by an I/Q demodulator, yielding two components (in-phase and the quadrature) of the demodulated signals.

10.6342/NTU201603287

The demodulated signals are then filtered using a low-pass filter. The filtered signals are finally sampled by the 12-bit analog to digital converters (ADC) with the sampling rate of about 36 kHz. The signals are stored on the SD memory card. Table 3.2 lists the parameters of the transmission and reception of the acoustic signal.

3.3 Hydrographic Survey

3.3.1 CTD

R/V ORIII is equipped with a CTD system of 9plus model from Sea-Bird Electronics, Inc [25]. The CTD sensors measure the vertical profiles of the temperature and conductivity. 13 CTD casts (triangles as shown in Figure 3.1) were conducted at the positions near the four moored stations and the waypoints of the tow track. The details of each CTD cast are listed in Table 3.3.

The properties of the seawater are represented following the standard of Thermodynamic Equation of Seawater 2010 (TEOS-10) [13]. TEOS-10 is a new standard adopted in June 2009 to replace EOS-80 [30] as an official description of seawater properties in marine science [31]. TEOS-10 is based on the Gibbs function formulation, and one of its advantages is that the sound speed of the seawater can be mathematically derived using the properties of the seawater (absolute salinity, conservative temperature, and pressure) with the Gibbs function. The previous practices usually apply empirical formulations, such as the equation given by Del Grosso [5]. To comply with TEOS-10, the conservative temperature and the absolute salinity are derived from the measured temperature and conductivity, respectively, using the subroutines in the Gibbs-SeaWater (GSW) Oceanographic Toolbox of TEOS-10. The conservative temperature is the ITS-90 standard conservative temperature with the unit of °C [24]. The absolute salinity with the unit of $\mathrm{g\,kg^{-1}}$ has replaced the practical salinity unit (PSU) in TEOS-10 because the absolute salinity can account for the effect of the dissolved materials on the properties of the seawater better than that of the PSU does. Note that the obtained absolute salinity was not directly measured but was estimated using the measured conductivity [14].

The conservative temperature and absolute salinity profiles are shown in Figure 3.9. The temperature profiles [Figure 3.9(a)] vary with time and it is relatively low near the sea surface for Casts 1–8. The salinity profiles [Figure 3.9(b)] show that low salinity is near the sea surface. The lowest salinity with the value of 31 $\mathrm{g\,kg^{-1}}$ was observed in Cast 8. The low salinity and temperature near the sea surface are due to heavy rain during the experiment. The rainfall provided the cool, fresh water

10.6342/NTU201603287

input to the sea. Also, the cloud blocked the radiation from the sun, reducing the heat flux to the sea water.

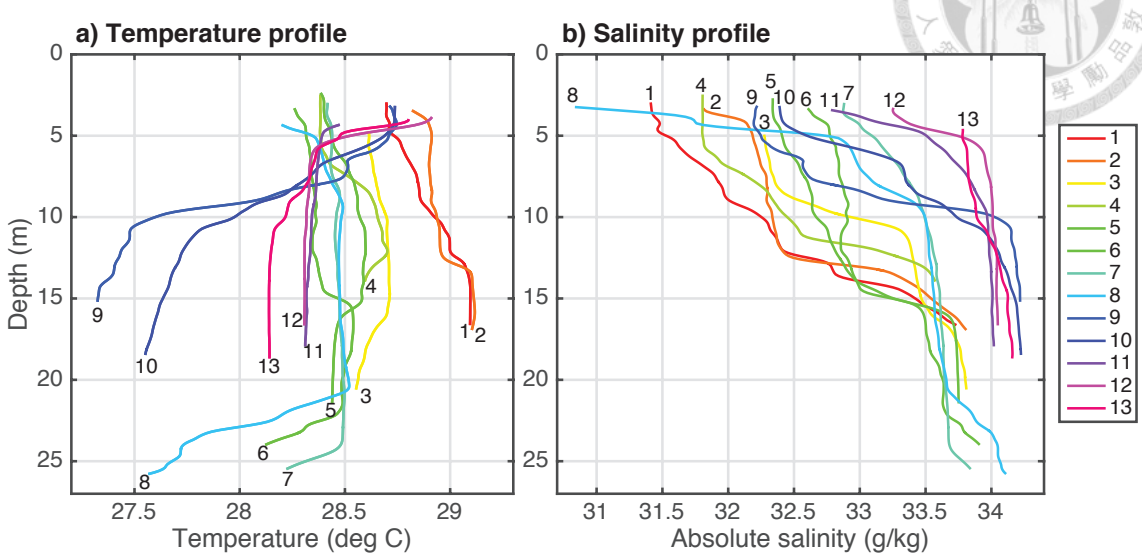

Figure 3.9: (a) Temperature and (b) absolute salinity profiles obtained from the CTD casts.

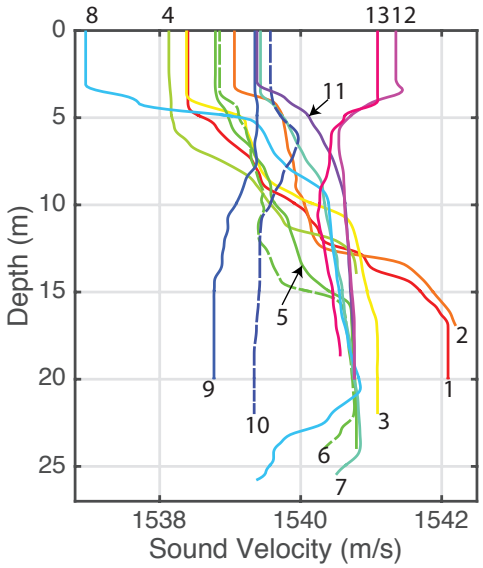

Figure 3.10: Measured sound speed profiles (SSPs) during the experiment.

The SSPs are computed from the conservative temperature and absolute salinity. The calculation is conducted using the Gibbs-SeaWater (GSW) Oceanographic Toolbox of TEOS-10. Later in Section 5.1, the measured SSPs are used to simulate the sound propagation via the ray tracing code BELLHOP [23]. The temporal and

10.6342/NTU201603287

Table 3.3: Location and time of CTD casts.

No.	Local time	Location	Longitude (°E)	Latitude (°N)
1	8-29 12:52	M1	120.1847	22.7647
2	8-29 15:13	M4	120.1855	22.7485
3	8-30 06:52	M2	120.1643	22.7697
4	8-30 16:24	WP1	120.1961	22.7573
5	8-30 16:49	M3	120.1629	22.7587
6	8-31 06:50	M3	120.1624	22.7612
7	8-31 09:49	WP3	120.1520	22.7645
8	8-31 12:36	WP3	120.1502	22.7658
9	9-1 16:06	M1	120.1892	22.7645
10	9-1 17:26	M4	120.1806	22.7489
11	9-2 06:59	M1	120.1850	22.7640
12	9-2 13:54	M1	120.1863	22.7639
13	9-2 18:10	M4	120.1798	22.7479

spatial variations of the SSPs are clearly seen in Figure 3.10. The SSPs obtained from Casts 1–8 (during the period from August 29 to 31) exhibit a similar characteristics: Due to low temperature and salinity near the sea surface, its sound speed was lower than the depth below, resulting in an upward refracting sound speed profile. The SSPs of Casts 12 and 13 (September 2) show the high sound speeds near the sea surface due to the high temperature of the surface water. The sound speeds decreased with depth and were relatively stable below the depth of 8 m. The SSPs of Casts 9 and 10 show the little vertical variation of about 0.6 $\mathrm{m\,s^{-1}}$.

The temperature, salinity and sound speed profiles as shown in Figure 3.9 and 3.10 are processed from the CTD measurements. In the raw data, some of the measurements near the sea surface (about 5 m from the surface) are scattered. These scattered measurements are removed. The rest of measurements are moving averaged along the depth axis with the window size of 0.5 m. The averaged profiles of temperature and salinity are shown in Figure 3.9.

In addition to the removal of the scattered data near the sea surface, the sea water near the sea floor were not sampled by the CTD sensors. Since the SSP is the input to the ray simulation model, the lack of the sound speed data near the sea surface and bottom is an issue. The missing data of the SSP are extrapolated using the existing data. The sound speed near the bottom usually changes little. Thus, it is linearly extrapolated from the bottommost measurements. For the sound speed at the surface, it is assumed that the sound speed is constant in the surface layer

10.6342/NTU201603287

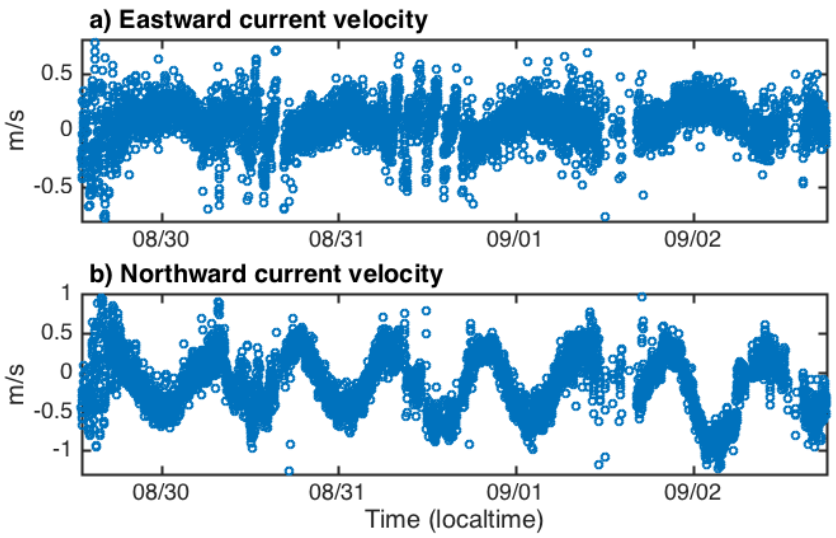

Figure 3.11: Time series of the current velocity in (a) eastward and (b) northward directions measured by the shipboard-ADCP.

due to the mixing process by the sea surface wave. The sound speed at the surface is then estimated from the validly shallowest measurements.

3.3.2 Shipboard ADCP

An Aquadopp current profiler from Nortek AS was deployed [19]. Unfortunately, the current profiler malfunctioned due to the improper setting of parameters. Therefore, the only direct measurement of the currents was obtained from the shipboard-ADCP on R/V ORIII. The shipboard-ADCP is a 75 kHz model of Ocean Surveyor family from Teledyne RD Instruments [27]. The ADCP measured the current velocity of the water column beneath the vessel. Considering the blanking distance of the transducer, the installation depth of the ADCP and the selected bin size (4 m), the depth of the first bin (the shallowest water mass that can be measured) is 14.7 m below the sea surface. Since the water depth varies from 20 to 26 m in the experiment site, only the upper one or two bins were reliable.

Note that the 75 kHz model ADCP might not be suitable to measure the currents in the shallow-water environment and that it is preferable for the research vessel to sail at a constant velocity. In general, the data quality increases with the larger bin size. The bin size of the ADCP was configured to 4 m due to a relatively shallow water depth.

Figure 3.11 displays the time series of the current measurements from the shipboard-ADCP. The ADCP continuously measured the currents during the en-

10.6342/NTU201603287

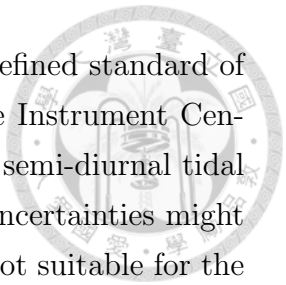

tire experiment. Some measurements were removed based on a defined standard of data quality. The data quality control was supported by Marine Instrument Center, Institute of Oceanography, National Taiwan University. The semi-diurnal tidal currents are clearly seen in the time series. The observed large uncertainties might be due to the following reasons: (1) the configured bin size was not suitable for the ADCP and (2) the research vessel sometimes did not sail at the constant velocity. Since the research vessel sailed around the experiment area, the time series of the ADCP-measured currents also exhibit the spatial variability.

3.4 Summary

This chapter summarized the field experiments conducted at the Sizhiwan Marine Test Field from August 29 to September 2, 2015. Four moored stations were deployed, and one mobile station was towed by the research vessel. The deployed stations measured the arrival patterns of the signals traversed from one station to another. Since the time accuracy of the measurements is critical for the data analysis, the instruments incorporate the accurate time sources from the GPS receiver to achieve high time precision. In addition to the travel-time measurements, the shipboard-ADCP provides the direct current measurements, and several CTD casts were conducted to obtain the SSPs in the experimental site. Next we shall use the collected data to estimate the currents.

10.6342/NTU201603287

Chapter 4

Data Analysis

The DTT data are fundamental to the acoustic mapping of ocean currents, since their magnitudes are proportional to the path-averaged current velocity. The DTT generally varied from 1 to −1 ms for the experimental configuration of this study, and the travel-time measurements need to resolve the small variation of the DTT. Conventionally, the DTT is estimated using the peak-picking method, which requires direct interpretation of the arrival patterns. It is usually difficult to apply the peak-picking method due to the complicated characteristics of acoustic propagation in the shallow-water channel. Another method, the waveform-matching method can mitigate the difficulties in picking the peaks. However, the method might produce incorrect estimates. In this study, we develop a method to improve the waveform-matching method.

Figure 4.1 summarizes the procedures for the DTT estimation. The Doppler processing is first applied to the raw data, yielding the delay-Doppler ambiguity function. From the ambiguity function, the Doppler shift of the signal and the relative velocity between transceivers are estimated. The arrival pattern associated with the estimated Doppler shift is obtained simultaneously. The signal-to-noise ratio (SNR) is also computed for each pattern to quantify the data quality. To estimate the DTT, we compute the cross-correlation function (CCF) between reciprocal patterns, which provides simpler interpretation of the DTT. The CCF exhibits multi-peak structure. Using the method proposed here, the appropriate peak in each CCF is selected. Finally, the lag time of the selected peak provides the estimate of the DTT.

10.6342/NTU201603287

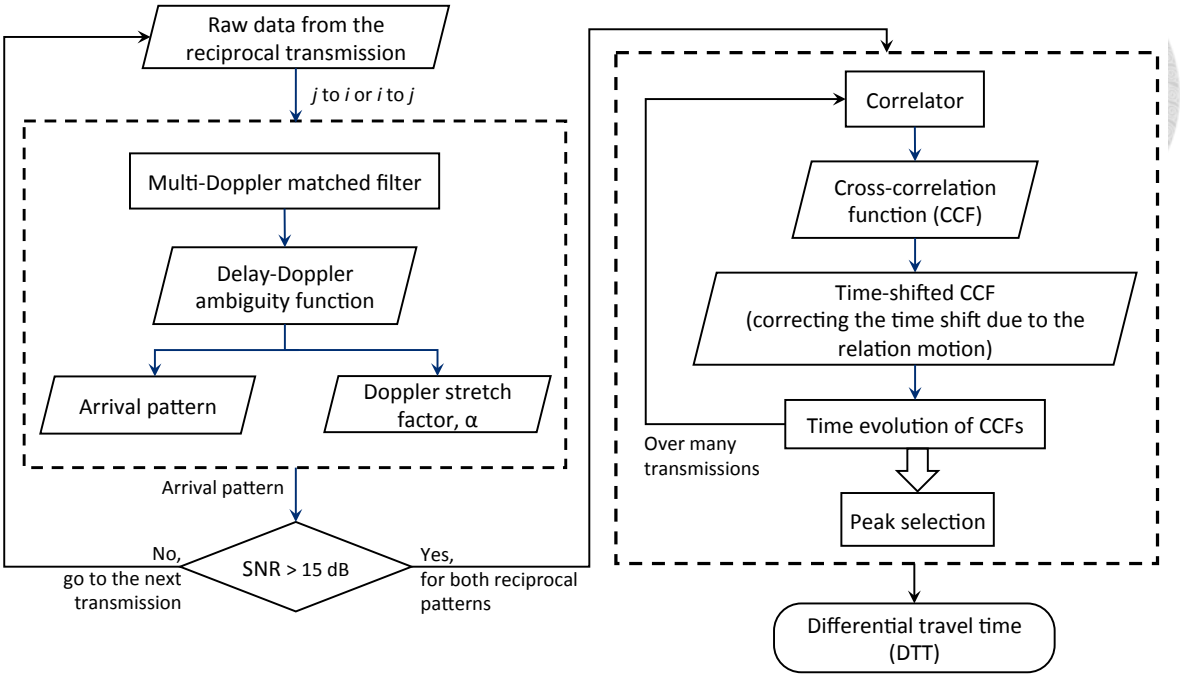

Figure 4.1: Flowchart of DTT estimation.

4.1 Raw Data

The raw data were downloaded from the acoustic stations. Each file stored in the memory card is an acoustic recording from one transmission test. As introduced in Section 3.2, the received signals are the two components of the I/Q demodulated (baseband) signals. The demodulated signals are sampled by the 12-bit ADCs with the sampling frequency of about 36 kHz. The parameters for the acoustic recording are listed in Table 3.2.

Figure 4.2 shows an example of the received signals. The recording began at 228 ms after the signal transmission and lasted about 3 s. The values are chosen so that the signals from all the remote stations can be recorded. Since the data have high SNR, it can be clearly seen that there are two incoming signals arrived at 874 ms and 1156 ms without further signal processing.

4.2 Doppler Processing

In the experiment, there exist motions of the acoustic transceivers: The transceiver towed by the ship was moved with the speed of about 1.5 $\mathrm{m\,s^{-1}}$. The transceiver for the moored station was suspended from the surface buoy and the transceiver might undergo some motion induced by to the sea surface wave or the dragging force of the

10.6342/NTU201603287

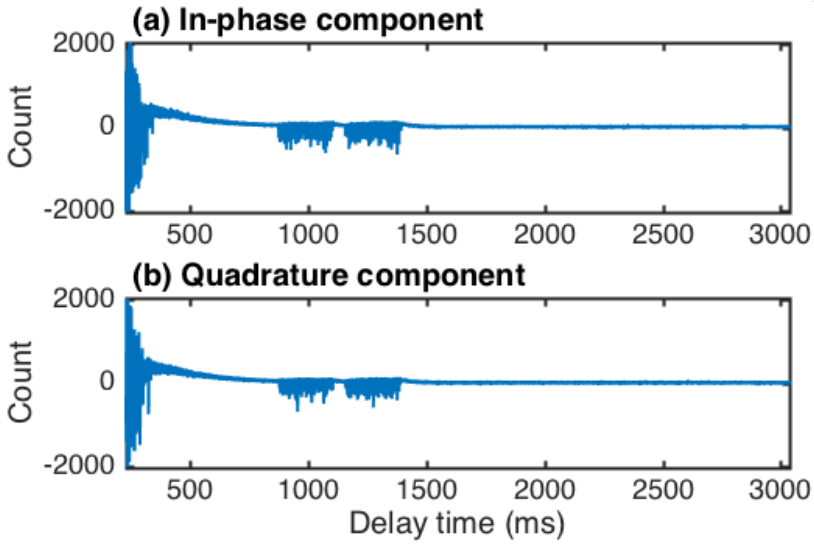

Figure 4.2: Raw data of the received acoustic signals (a) in-phase and (b) quadrature components.

surface currents. Due to the relative motion between the transceivers, the received signals in the experiment were affected by the Doppler effect.

To obtain the acoustic arrivals from the signal distorted by Doppler shifts, Figure 4.3 demonstrates the Doppler compensation scheme applied to the experimental data. The signal was transmitted from M1 (moored station) and was received at M5 (towed station). Figure 4.3(a) shows the wideband delay-Doppler ambiguity function in dB scale. The relative velocity u_{r} is used to represent the Doppler axis. There exist multiple arrivals with different Doppler factors, and the arrival with maximum magnitude is at the $u_{\mathrm{r}} = 1.46\ \mathrm{m\,s^{-1}}$ and $\hat{\tau} = 1139$ ms [the red plus sign in Figure 4.3(a)].

For the signals sensitive to Doppler shift, the Doppler processing is required before the matched filtering: The replica of the transmitted signal should be Doppler-shifted according to the estimated Doppler. The acoustic arrivals are then recovered by matched filtering the received signal with the Doppler-shifted replica. The arrival pattern is defined as the envelope of the matched-filter output.

Compared with the arrival pattern without the Doppler processing [the dotted line in Figure 4.3(b)], the acoustic arrivals can be seen clearly after the processing (solid line). The processed waveform is the horizontal slice passing through the maximum [the white line in Figure 4.3(a)]. Note that the arrival patterns plotted in Figure 4.3(b) are in the linear scale.

The Doppler shift estimated from the moored pair is low compared to that from the moored-towed pair. Although the acoustic arrivals between the moored stations

10.6342/NTU201603287

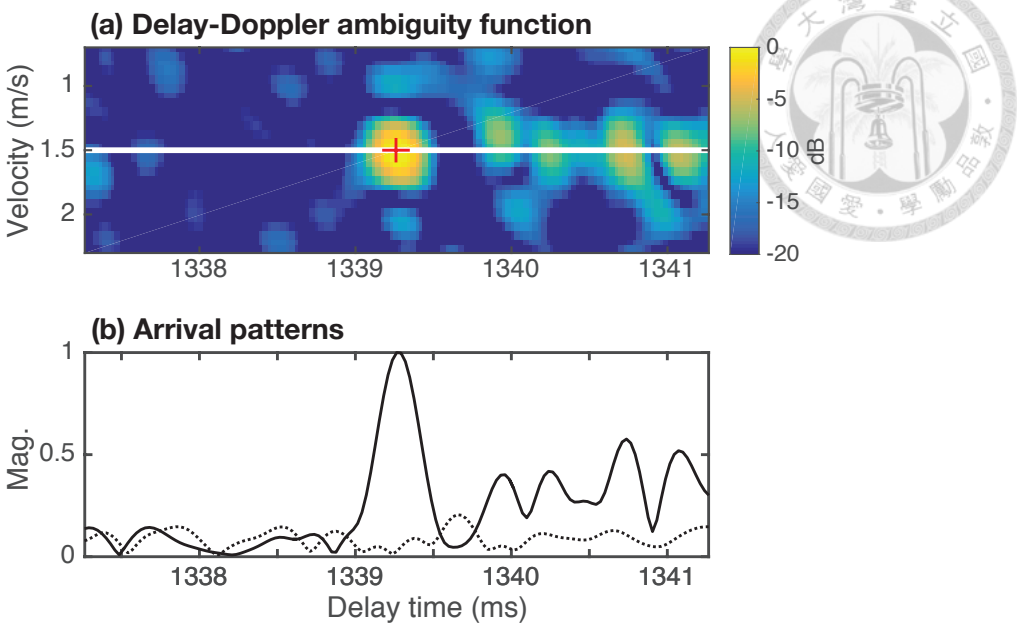

Figure 4.3: An example of the processed data after compensating for the Doppler shift. (a) The delay-Doppler ambiguity function of the received signal. (b) The arrival patterns with (solid line) and without (dotted line) compensating Doppler. The data are from the acoustic transmission from M1 to M5 at 7:57 am on August 31 (local time).

are revealed without the Doppler processing, the SNR of the arrival pattern can be improved using the further processing. Therefore, the Doppler processing is applied to all the collected acoustic data.

For the current estimation using the towed transceivers, one needs to estimate the motion of the instrument using the obtained Doppler factor. Consider the acoustic transmission between the stationary station with the velocity $u_1 = 0$, and the towed station with the velocity u_2 (along the direction $\mathbf{r}_{12}$). The velocity of the towed station can be determined by the Doppler estimation $u_2 = -u_\mathrm{r}$. Note that the negative sign is due to different definitions used for the velocity directions.

Figure 4.4 shows the time series of the estimated (radial) velocity for the towed station M5. The time interval is from 13:38 to 16:08 on August 30 (local time). The blue and red circles indicate the Doppler estimated velocities using the signals transmitted from M1 to M5 and from M5 to M1, respectively. The yellow cross symbol is the estimate using the GPS position measurements with the sampling interval of 30 s. The sudden change of the estimated velocity is due to the changing course of the ship at the waypoints. The two estimates show a consistent trend. The GPS-based estimate is the average velocity over the sampling interval (30 s)

10.6342/NTU201603287

while the Doppler-based estimate is the instantaneous velocity. Thus, the motion of the towed station is estimated using the Doppler-based estimate in the following analysis.

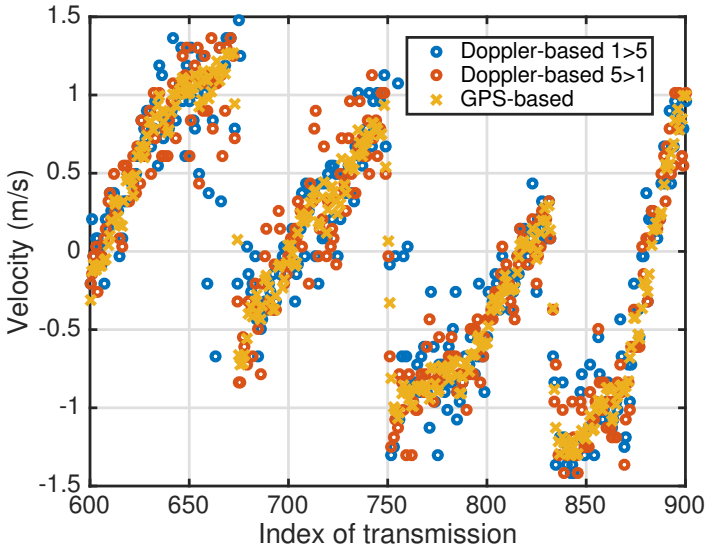

Figure 4.4: Time series of the estimated velocity for the towed station M5.

4.3 SNR Calculation

In order to quantify the quality of the arrival pattern, the signal-to-noise ratio (SNR) is defined as follows:

$$\mathrm{SNR} \equiv \frac{y_{\mathrm{s}}^2}{\langle y_{\mathrm{n}}^2 \rangle}, \tag{4.1}$$

where y_{s} is the amplitude of the maximum peak in the matched filter output and $\langle y_{\mathrm{n}}^2 \rangle$ is the output variance due to noise only. The SNR is represented in dB scale. In general, there exist multiple arrivals with the time span less than 10 ms. The estimation of $\langle y_{\mathrm{n}}^2 \rangle$ should avoid the arrival pattern in the interval that contains the arrivals. Figure 4.5 illustrates the calculation of the SNR using a measured arrival pattern. The time interval centered at the maximum peak with the width of about 11 ms is taken as the time spread of multipath arrivals. The average power in the time intervals of 50 ms, before and after the centered interval (gray area in Figure 4.5), is used to estimate noise variance $\langle y_{\mathrm{n}}^2 \rangle$.

Because the energy of the acoustic signal is spread into multiple arrivals, the SNR calculated in this study might be underestimated. The arrival pattern with SNR lower than 15 dB is removed from the further analysis.

10.6342/NTU201603287

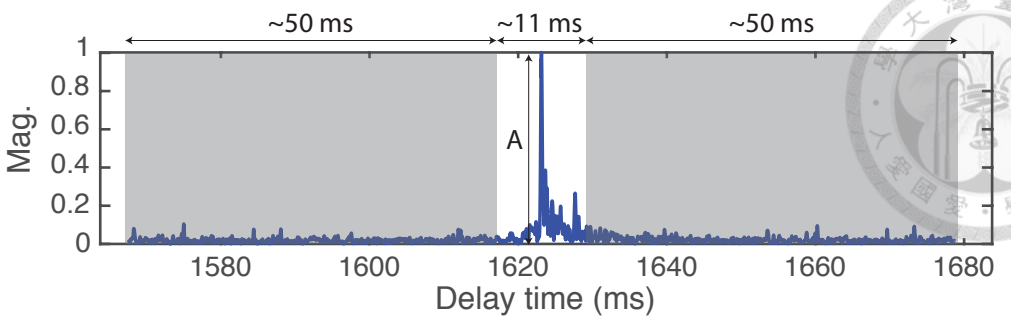

Figure 4.5: Definition of the SNR for an arrival pattern.

4.4 Time-evolving Cross-Correlation Function for Reciprocal Arrival Patterns

Before proceeding to this step, the two methods for estimating the DTT are reviewed. The two methods are referred to as the peak-picking and the waveform-matching methods [2].

- Peak-picking method
  To apply the method, the reciprocal arrivals in the reciprocal patterns are paired. The paired peaks have similar shapes, amplitudes, and arrival times. The DTT is then determined using the difference between the arrival times of the paired peaks. Figure 4.6(a) illustrates the peak-picking method applying to the reciprocal arrival patterns collected in the experiment. The two maximum peaks in each pattern are paired. The DTT is estimated using the difference between the arrival times of the peaks.

- Waveform-matching method
  Figure 4.6 illustrates the waveform-matching method. To apply this method, the cross-correlation function (CCF) [Figure 4.6(b)] between reciprocal arrival patterns [Figure 4.6(a)] is computed. The DTT is determined using the lag time at which the CCF reaches to the maximum. The limitation of the waveform-matching method is that the DTTs for individual arrivals are not available.

Conventionally, the DTT is estimated using the peak-picking method. Due to the complicated propagation features in the underwater channel it is usually difficult to pair reciprocal peaks for the peak-picking method. The difficulties can be mitigated using the waveform-matching method because the pairing process is avoided.

10.6342/NTU201603287

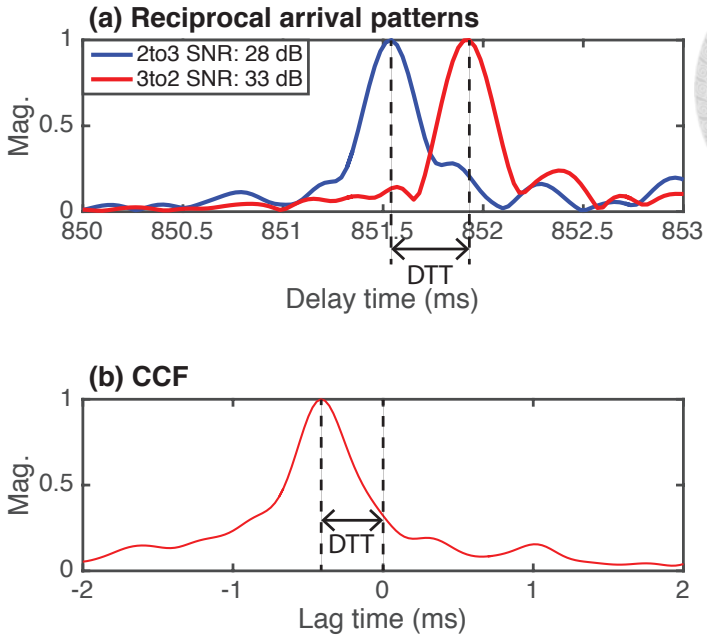

Figure 4.6: Estimations of DTT using (a) the peak-picking and (b) the waveform-matching methods.

Although the waveform-matching method can mitigate some issues, this method may not work properly sometimes. In general, the magnitude of the CCF is small and the CCF has multiple peaks due to the multiple arrivals. Each peak in the CCF corresponds to the alignment of acoustic arrivals in reciprocal patterns. Ideally, the reciprocal arrivals have similar patterns with slightly different arrival times, resulting from the current effect, and the DTT can be estimated successfully by the lag time at which the CCF reaches the maximum. However, the maximum could sometimes lead to the incorrect estimate of DTTs. A reasonable estimate of DTT should consider all the potential peaks in the CCF and select the one which is persistently present over time.

Figure 4.7 shows an example of (a) the reciprocal patterns and (b) the resulting CCF from the measured data. In Figure 4.7(a), the red pattern denotes the signal traversed from M2 to M1 while the blue denotes that of the opposite direction. The SNRs of both patterns are 23 dB and 25 dB, respectively. Each pattern is normalized by the amplitude of the maximum arrival. There are four arrivals (R1, R2, B1, and B2) identified in Figure 4.7(a), and these arrivals can be categorized by two pairs of reciprocal arrivals: the R1-B1 and the R2-B2 pairs. Note that the magnitude of R1 is far smaller than that of B1. In Figure 4.7(b), each peak in the CCF is denoted by a number. Although Peak 4 has the maximum magnitude among all, it corresponds

10.6342/NTU201603287

to the alignment of the R2-B1 pair. It is reasonable to estimate the DTT using the lag time of Peak 5 than that of Peak 4, since Peak 5 corresponds to the alignment of the two reciprocal arrival pairs (the B1-R1 and the B2-R2 pairs).

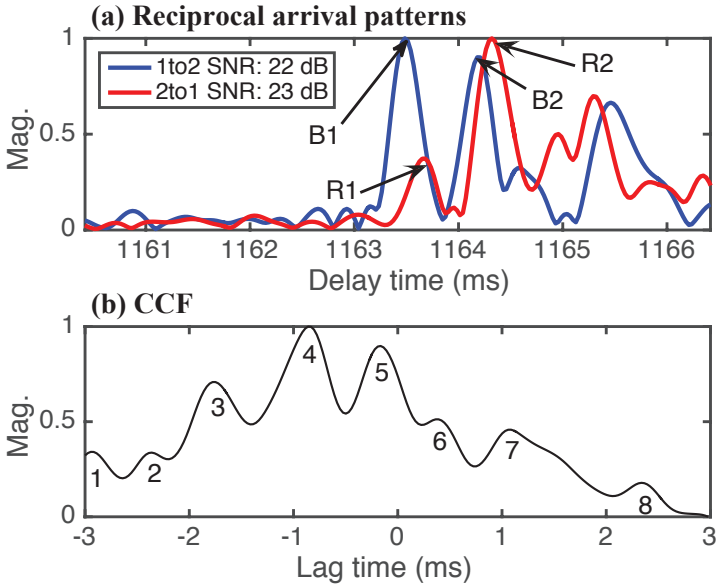

Figure 4.7: (a) Reciprocal arrival patterns. (b) The corresponding CCF.

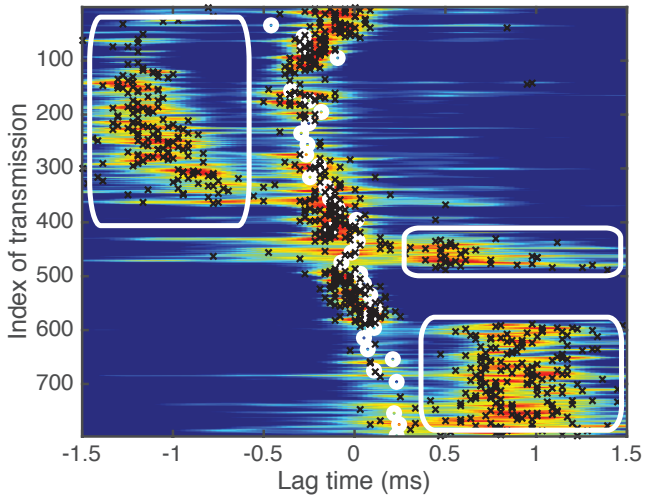

Figure 4.8: Time-evolution of the CCFs. The data are from reciprocal transmission between M1 and M2. The transmission began at 16:21 on August 30 (local time) with the transmission interval of 30 s.

To address the above issue, we select the peaks based on the time-variation of the CCFs as shown in Figure 4.8. Each CCF (the horizontal slice) is averaged

10.6342/NTU201603287

over 5 adjacent CCFs and then normalized by the maximum. The average process reduces random fluctuations and enhances the trend of the peaks in CCFs. The black cross symbol indicates the maximum peak in the CCF before the average, and the white circle is the predicted DTT calculated from the current velocity measured by the ADCP. We see that the lag time of the maximum peaks agrees well with the predicted DTT, except for the peaks inside the white rectangles. The trend of those peaks is inconsistent with that of the rest peaks due to the reason mentioned in the discussion for Figure 4.7. The time-variation of the CCFs can be used to track the appropriate peaks for the determination of DTT.

Before analyzing the CCFs obtained from the reciprocal transmission between a moored station i and a towed station j, it is preferable to time shift these CCFs to compensate for the offset induced by the instrument motions. As stated in Equation (2.4):

$$\Delta t_{ij} = -\frac{2R}{c^2} v_{\mathrm{m}} - \frac{R}{c^2} u_{\mathrm{r}}. \tag{4.2}$$

The DTT Δt_{ij} measured between the moored and towed stations depends on not only the path-averaged current velocity v_{m} but the relative velocity u_{r}. Since the DTT estimation involves tracking the pattern in the CCFs, a new variable $\Delta\tilde{t}_{ij}$ correcting for the effect of the relative velocity is defined as follows:

$$\Delta\tilde{t}_{ij} \equiv \Delta t_{ij} + \frac{R}{c^2} u_{\mathrm{r}} \tag{4.3}$$

$$= -\frac{2R}{c^2} v_{\mathrm{m}}. \tag{4.4}$$

The new variable $\Delta\tilde{t}_{ij}$ depends only on v_{m} and hence shows a small variation. The variable $\Delta\tilde{t}_{ij}$ is estimated using the time-shifted CCF

$$\widetilde{\mathrm{CCF}}(\tau) = \mathrm{CCF}\left(\tau - \frac{R}{c^2} u_{\mathrm{r}}\right), \tag{4.5}$$

where τ indicates the lag time. Figures 4.8(a) and 4.8(b) show the time evolution of the original and the time-shifted CCFs, respectively. After shifting the time axis, we can see that temporal variation of the CCFs [Figure 4.8(b)] is reduced. Thus it is easier to track the pattern in the time-shifted CCFs for the estimation of $\Delta\tilde{t}_{ij}$. Despite the smaller time variation, the peak pattern in Figure 4.8(b) still exhibits discontinuities, e.g., the transmission index of around 225. The existence of the discontinuities is due to the sudden change in the angle of the ray path. The white dashed lines indicate the times when the ship changed course. The gaps in the pattern, e.g., the indices from 330 to 380, are due to the long distance in the acoustic transmission.

10.6342/NTU201603287

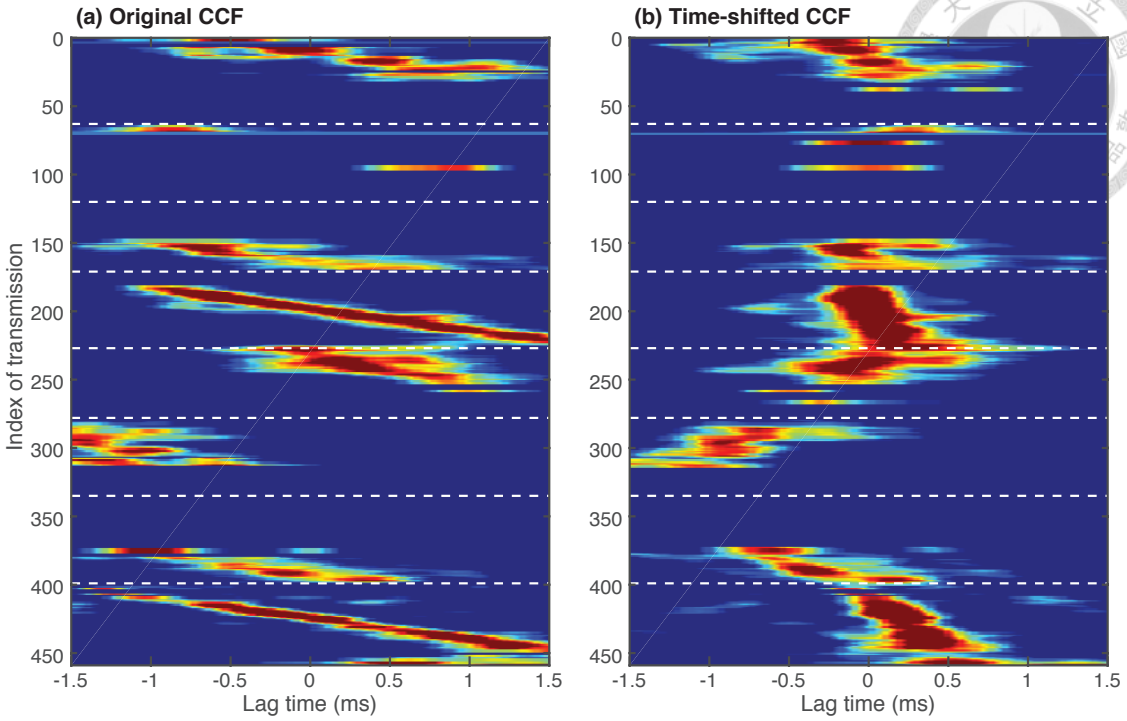

Figure 4.9: Time evolution of the (a) original and (b) time-shifted CCFs. The data are from the pair M2–M5 during the period beginning at 10:40:30 on September 2 with a transmission interval of 30 s. Each CCF (one horizontal slice) is obtained by averaging over five adjacent CCFs.

4.5 DTT Estimation

The lessons learned in Section 4.4 is that the highest peak in the CCF could sometimes lead to an incorrect estimate of the DTT. Therefore, it is necessary to select the appropriate peak in the CCF instead of selecting the highest one. A method is developed for the selection of the peaks in the CCF. The proposed method is composed of three steps: pre-processing, prediction, and estimation.

In the pre-processing step, one observes the trend in the CCF and remove some of the peaks from the consideration. The removed peaks are those exhibit inconsistent trend with the overall trend in the CCF. One typical example of the removed peaks are the ones inside the white rectangles in Figure 4.8. These peaks exist due to the reasons discussed in Figure 4.7. Figure 4.10(a) shows one realization of this step with a time-evolution of the CCF and the peaks in the CCFs. The removed and remained peaks are denoted by the dark and the white circles, respectively. The CCFs in the first 250 transmissions show high intensities at the lag time of about 0.4 ms. However, we see that high intensities near the 300 th transmission

10.6342/NTU201603287

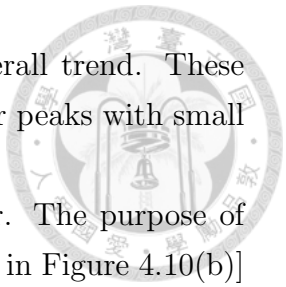

are located at the lag time around 1 ms, deviated from the overall trend. These deviated peaks with high amplitude are removed along with other peaks with small magnitudes.

The steps of prediction and estimation are jointed together. The purpose of the prediction step is to provide predictions of DTTs [the red line in Figure 4.10(b)] that guide the selection of the peak in CCF. In the estimation step, the peaks in the CCF are examined, and the one closest to the predicted DTT is selected. For example, the DTT for the 300th transmission can be predicted using the determined DTT from the 290th to 299th transmissions. Following the time evolving CCFs the predicted DTT at the 300th transmission should be at about 0.4 ms, instead of 1.0 ms that corresponds to the maximum value in the CCF. Then, all the peaks, remained in the pre-processing step, in the 300th CCF are examined [the gray circles in Figure 4.10(b)]. The selection of peak is based on the criteria listed below:

- The magnitude of the peaks should be higher than 0.6.
- The difference between the lag time of the peak and the predicted DTT should be smaller than 0.1 ms.
- If there exist multiple peaks satisfying the above criteria, the one that is closest to the predicted DTT is selected.

If a peak is selected, the DTT is estimated using the lag time of the selected peak [the white circle in Figure 4.10(b)]. A new process of the prediction and estimation steps is applied to the data from the next transmission.

4.6 Summary

In this chapter we presented the procedures for extracting differential travel time (DTT) from the raw acoustic data. To improve the SNR of the arrival pattern (the matched filter output), the Doppler signal processing based up the delay-Doppler ambiguity function was employed to all the collected data. For the estimation of DTT from the reciprocal patterns, we devised a robust method that tracks the DTTs continuously using the time-evolution of the CCFs. The obtained DTTs shall be used to estimate the current field in the study area in the next chapter.

10.6342/NTU201603287

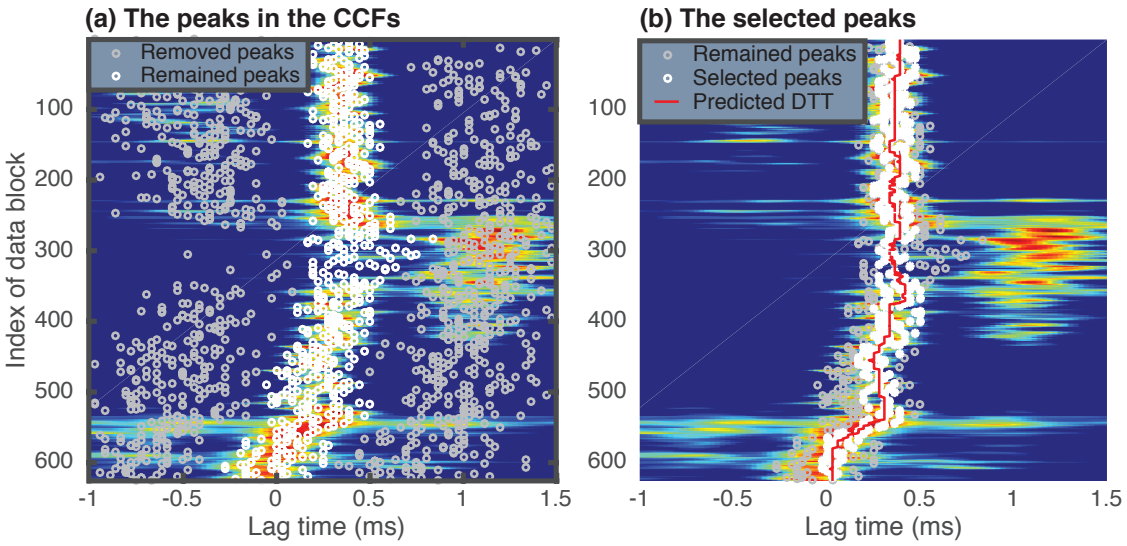

Figure 4.10: Illustration of the DTT estimation using the time evolution of the CCFs for the moored pair. (a) Removed (gray circle) and remained (white circle) peaks. (b) The selected peaks (white dot), the remained (gray circle) peaks [same as the white circle in (a)], and the predicted DTTs (red line). The background of (a) and (b) is the time-evolution of the CCF. The data were collected from Pair M1–M2 in the period beginning at 11:08 on August 30 with the transmission interval of 30 s.

10.6342/NTU201603287

Chapter 5

Results and Discussion

5.1 Eigenray Simulations

The purpose of eigenray simulations is to investigate what portion of the water column was sensed by the acoustic waves in order to gain an insight into the interpretation of the path-average current velocity obtained by the reciprocal transmission.

The input parameters for the ray model include the sound speed profile obtained from the CTD casts, the transceiver depths from the co-located pressure sensors, the horizontal distance between the transceivers estimated from the GPS positions, the bathymetry data from Ocean Data Bank of the Ministry of Science and Technology, Republic of China [21], and the properties of the sea floor (Table 5.1) based on the previous study in the experiment site [35].

Table 5.1: Sea floor properties used in the BELLHOP simulations.

Compression sound speed	1615
Compression sound attenuation	0.3 dB wavelength^{-1}
Density	1.95 g cm^{-3}

Using the above environmental parameters, BELLHOP simulates eigenrays in the acoustic transmission. Figure 5.1 shows the simulation results in the acoustic channel between M2 and M4. The results show various attributes of the eigenrays, including the arrival times, launching angles [Figure 5.1(f)], amplitudes [Figure 5.1(g)], and propagation paths [Figures 5.1(b)–(e)]. From the arrival times and amplitudes of the arrivals, the synthesized waveform is obtained [Figure 5.1(h)] by convoluting the arrival patterns with the autocorrelation function of the transmitted signal [22]. The eigenrays with the launching angle larger than 5° are not simulated for their small arrival amplitudes: the energy of these eigenrays is largely dissipated

10.6342/NTU201603287

in the bounces at both the sea surface and seafloor.

The ray arrivals in Figure 5.1(f) are categorized into five groups, Group 1–Group 5, based on their arrival times. The eigenray paths for Groups 1 and 2 are indicated by the dashed and solid lines in Figure 5.1(b), respectively. The eigenray paths for Groups 3–5 are shown in Figures 5.1(b)–(e), respectively. We see that most of the eigenrays propagate through the entire water column and interact with both the bottom and surface boundaries. However, for these rays interacting with only one boundary (either the bottom or surface), such as the eigenrays of the orange dashed line in Group1, the red line in Group 2, and the orange line in Group 3, their amplitudes are relatively small compared with the other propagation paths.

The dominant arrivals shown in Figure 5.1(h) are those eigenrays of Group 3. Except for the weak arrival [the orange line in Figure 5.1(e)], the lines colored in green, purple, blue, and black all travel through the entire water column. Although the dominant rays might vary with the space and time due to the changes of ocean sound speeds, the rays usually travel through the entire water column.

Note that the arrival time of the peak is sensitive to the distance between the transceivers, which is not precisely known in the experiment. Figure 5.2 shows the arrival patterns for different horizontal distances between the transceivers. We found that, except for a time shift, in this environment the distance perturbation does not alter the arrival patterns too much. The synthesized pattern was compared with the measured (Figure 5.3). The measured patterns (blue) were time shifted so that the maximum peaks in both the measured and synthesized patterns are aligned in the time axis. Some similarities were observed between these two patterns without invoking the waveform inversions.

5.2 Description of the Measured Data and Estimated Currents

Figures 5.4 and 5.5 show the time series of (a) the SNR for the measured arrival pattern and (b) the DTT estimated from the reciprocal arrival patterns for each pair. At each transmission two SNR estimates are obtained for the reciprocal arrival patterns between any station pair, but only the lower SNR is plotted. The arrival patterns with SNR lower than 15 dB are removed. The time series of the SNR is further smoothed by the 61-order moving average filter. Most of the data from the transmissions between the moored stations [Figure 5.4(a)] have SNRs higher than 15 dB. The SNR of the arrival patterns between M1–M2 and the M1–M4 pairs drop

10.6342/NTU201603287

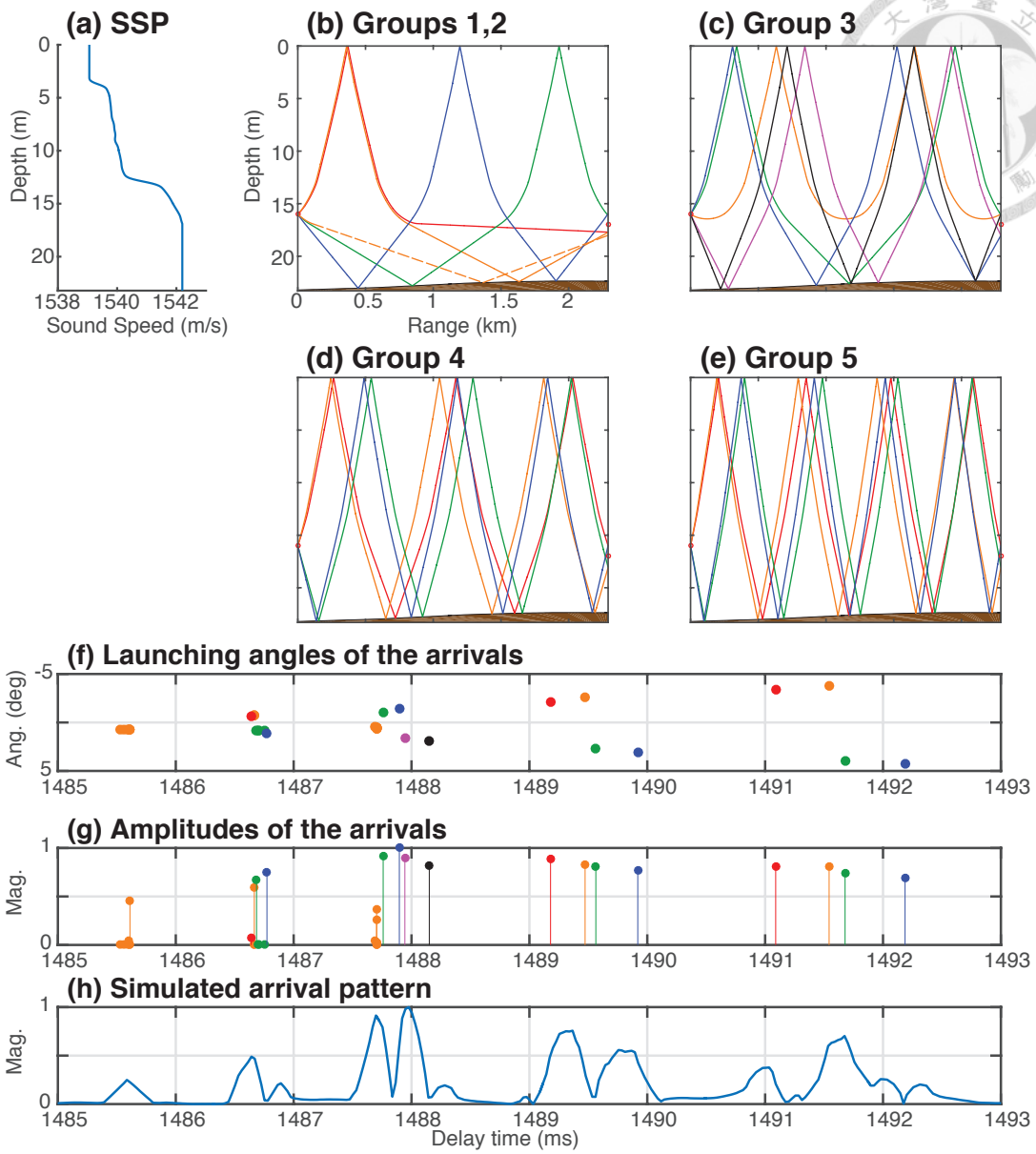

Figure 5.1: (a) Sound speed profile. (b)–(e) Eigenray paths. (f) Launching angles and (g) amplitudes of the eigenray arrivals. (h) Synthesized arrival pattern.

at about 40 hours. Then, the data obtained from M1 show low SNRs except for a temporal recovery at about 50 hours. The SNRs of the signals from the M1–M3 pair are not plotted in Figure 5.4 since no acoustic link between the stations.

Figure 5.6 shows the estimated current velocity (blue line) in (a) northward and (b) eastward directions with their corresponding error bars (light blue area). To reduce the uncertainties of the estimates, the DTTs are first processed by an 11th order (5 min) median filter. The black line indicates the *in-situ* current derived from the shipboard-ADCP measurement with the corresponding error bar (gray area). The shipboard-ADCP measurements exhibit a large variability when the

10.6342/NTU201603287

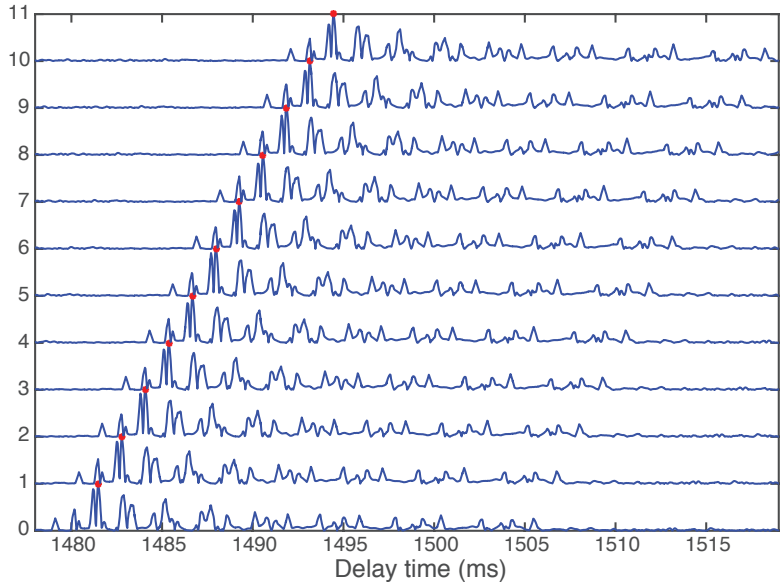

Figure 5.2: Synthesized arrival patterns with different horizontal distances between the transceivers.

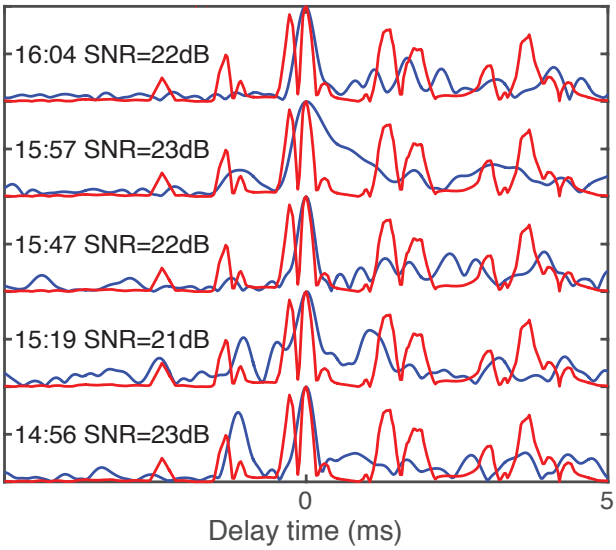

Figure 5.3: Synthesized (red) and measured (blue) arrival patterns.

R/V ORIII cruised along the planned track (Figure 3.1), and these measurements are not plotted. The time series of the measured velocity is moving averaged with the window size of 10 min. Figure 5.6 shows that the currents in the experiment site were dominant by the semi-diurnal tidal currents. The principal axis of the currents is along the isobaths (along-shore direction). The current is strong in the along-shore direction with the maximum magnitude of about 77 $\mathrm{cm\,s^{-1}}$ and is weak in the cross-shore direction with the maximum magnitude of about 23 $\mathrm{cm\,s^{-1}}$.

10.6342/NTU201603287

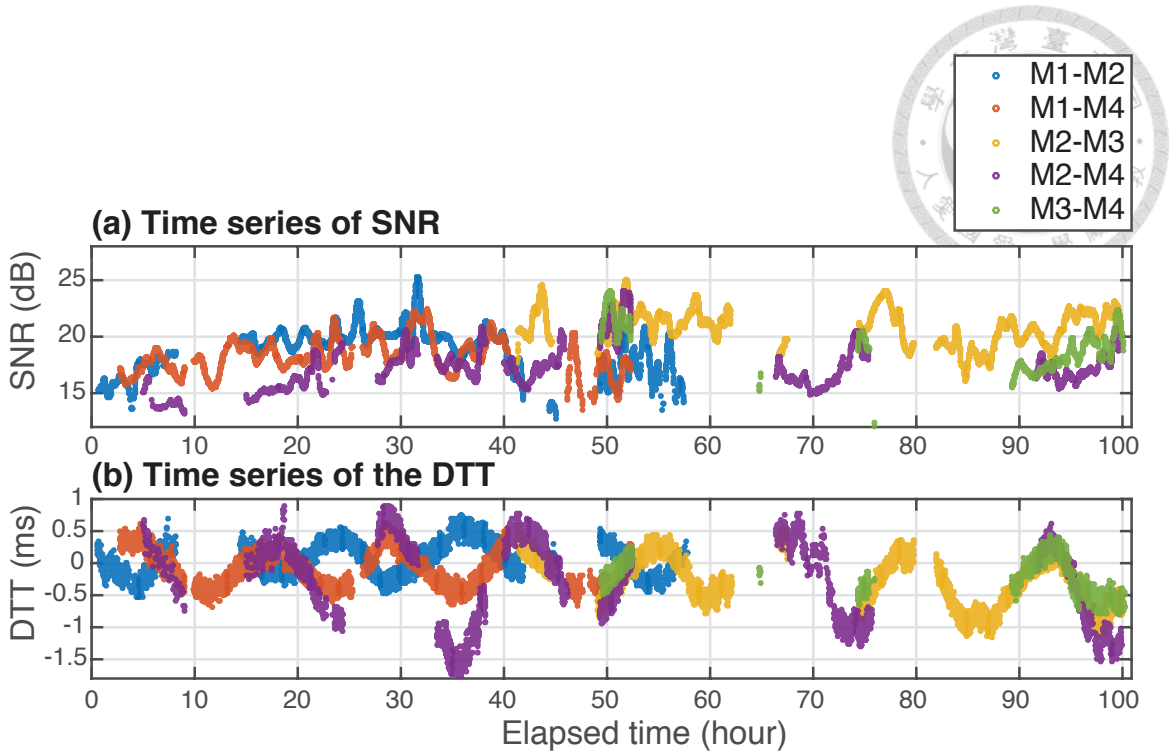

Figure 5.4: Time series of the (a) SNR and (b) DTT for the acoustic data collected between the moored stations. The horizontal axis is the elapsed time in hours from 13:12 on August 29, 2015.

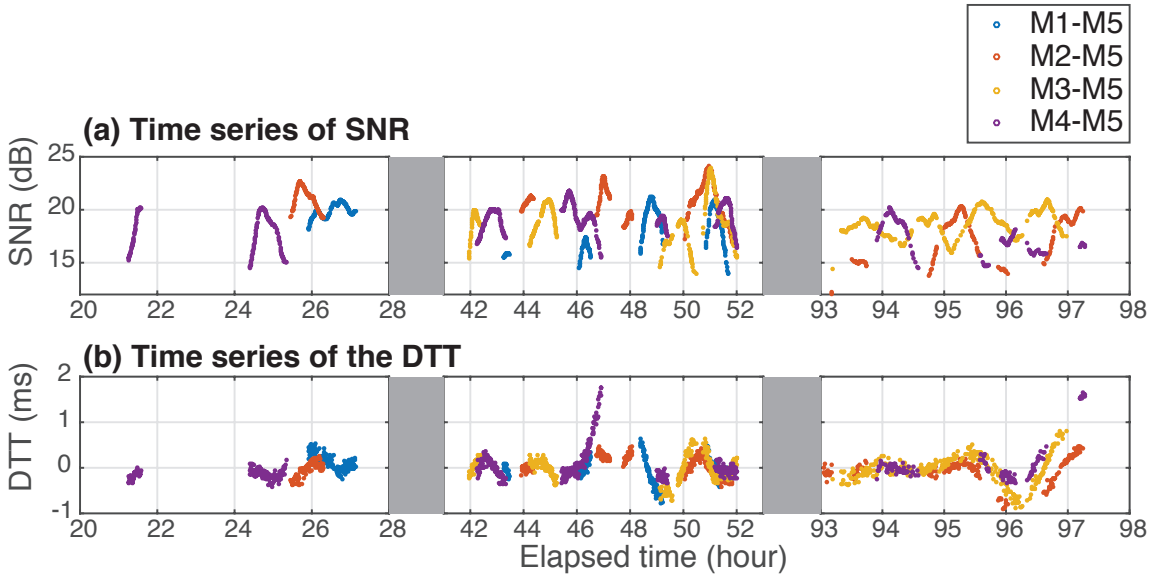

Figure 5.5: Time series of the (a) SNR and (b) DTT for the acoustic data collected between the moored and towed stations. The horizontal axis is the elapsed time in hours from 13:12 on August 29, 2015.

The depth variation of the currents in the experiment site should be small, as indicated by a previous survey in June of 2015 using an upward-looking 600 kHz

10.6342/NTU201603287

ADCP (Aquadopp profiler from Nortek AS [19]). The standard deviation of the current velocities at all depths (6 cells) is about 6.8 $\mathrm{cm\,s^{-1}}$ in the northward direction and is about 5.9 $\mathrm{cm\,s^{-1}}$ in the eastward direction. Hence, we assume that the current velocity measured by the shipboard-ADCP at the depth of about 15 m (due to the limitations of the cell size and the blanking distance) should be representative for the water column.

Since the R/V ORIII was cruising in the study site during the experiment, the time series of the ADCP shipboard data might contain the spatial variation (in the horizontal plane) of the currents. However, the spatial variation of the current field is usually small, as indicated by the estimated current field shown in Figures 5.7 and 5.8. Therefore, the spatial variation should not contribute much to the time series of the currents.

For the results of the acoustic mapping, the time series of the estimated currents agree well with the measurements from the ADCP. The time series of the estimated velocity also reveals the temporal patterns of the tidal cycles. The root mean square differences between the estimated and the ADCP measured velocities are 12 $\mathrm{cm\,s^{-1}}$ and 7 $\mathrm{cm\,s^{-1}}$ for the northward and eastward directions, respectively. The averaged error bars of the acoustic mapping are 6 $\mathrm{cm\,s^{-1}}$ and 6 $\mathrm{cm\,s^{-1}}$ for the northward and eastward directions, respectively. The averaged error bar of the ADCP measurements is 8 $\mathrm{cm\,s^{-1}}$.

Figures 5.7(a)–(m) and 5.8(a)–(g) display the snapshots of the estimated current fields. The arrow symbol inside the region enclosed by the ray paths denotes the current vector of the estimated field. The arrow at the left bottom represents the averaged current vector, which is the velocity shown in the time series of Figure 5.6. The color map provides the error map of the estimated field. The arrows in red and in orange represent the current vectors from the earlier and latter snapshots, respectively. The circles represent the stations. Each square represents the towed station at the latter snapshot, e.g., the square in Figure 5.8(a) denotes M5 station at Snapshot 30. The solid line shows the ray path used for the inversion.

Figures 5.7(h) and 5.8(n) show the time evolution of the current velocity at the snapshots shown in Figures 5.7 and 5.8, respectively. Each vertical dashed line denotes the time of a snapshot of the field. The number below the vertical line denotes the index of the snapshot.

As discussed in Figure 5.6, the current is stronger in the along-shore direction than in the cross-shore direction. The spatial variation of the currents is usually small except for the certain periods. The spatial variation of the currents in Snap-

10.6342/NTU201603287

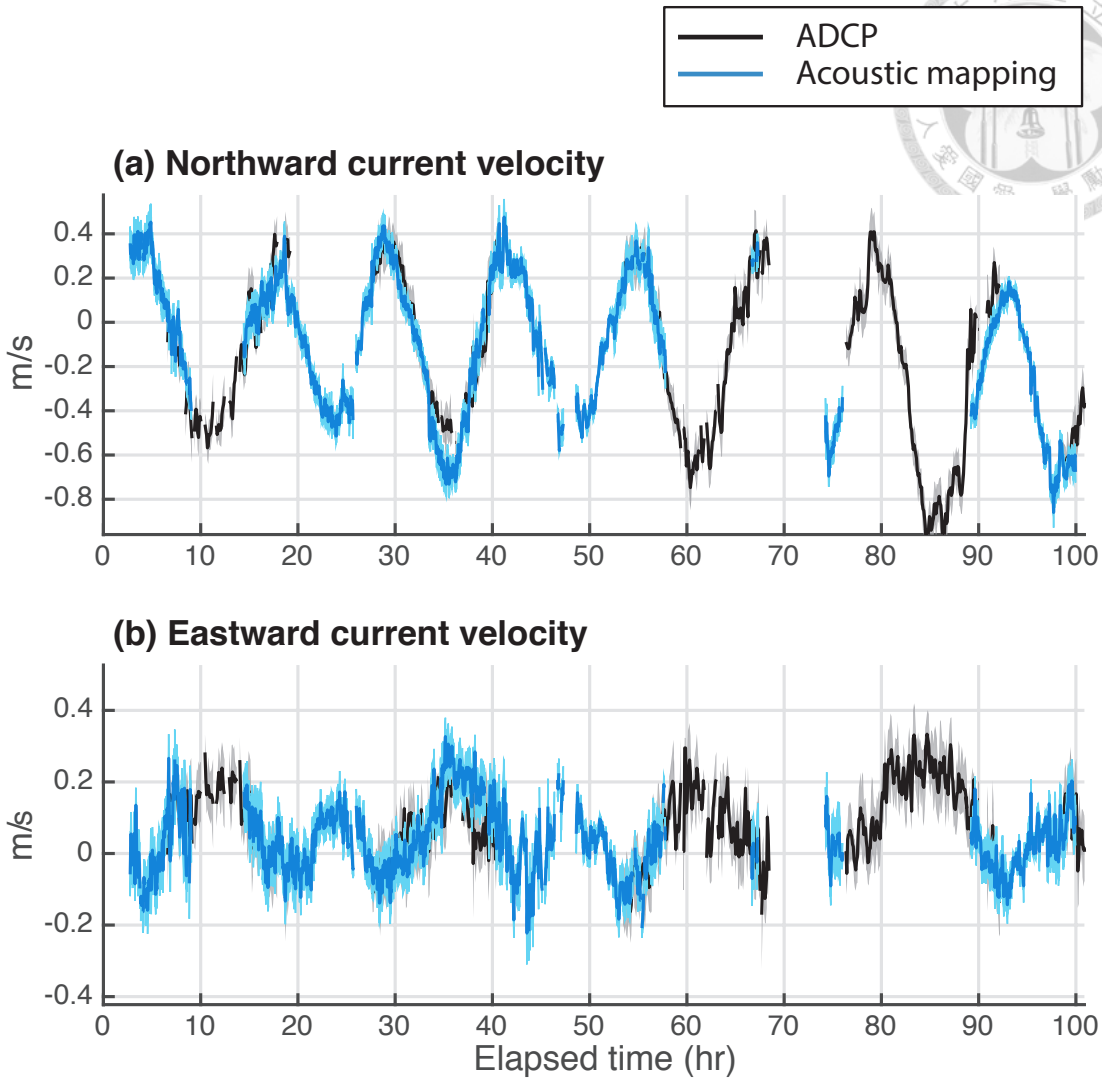

Figure 5.6: Time series of the current velocity from acoustic mapping (blue line) and the ADCP (black line) with their corresponding error bars (the light blue area for the results of acoustic mapping and the gray area for the ADCP measurements).

shots 17–28 is higher than the rest snapshots. These snapshots display the current distribution when the tidal currents change direction. During the period of Snapshots 17–28, the cross-shore current in the south area is stronger than that in the north. Snapshots 29–42 display the estimated fields while towing the transceiver. The coverage of the acoustic rays was increased by the towed station.

10.6342/NTU201603287

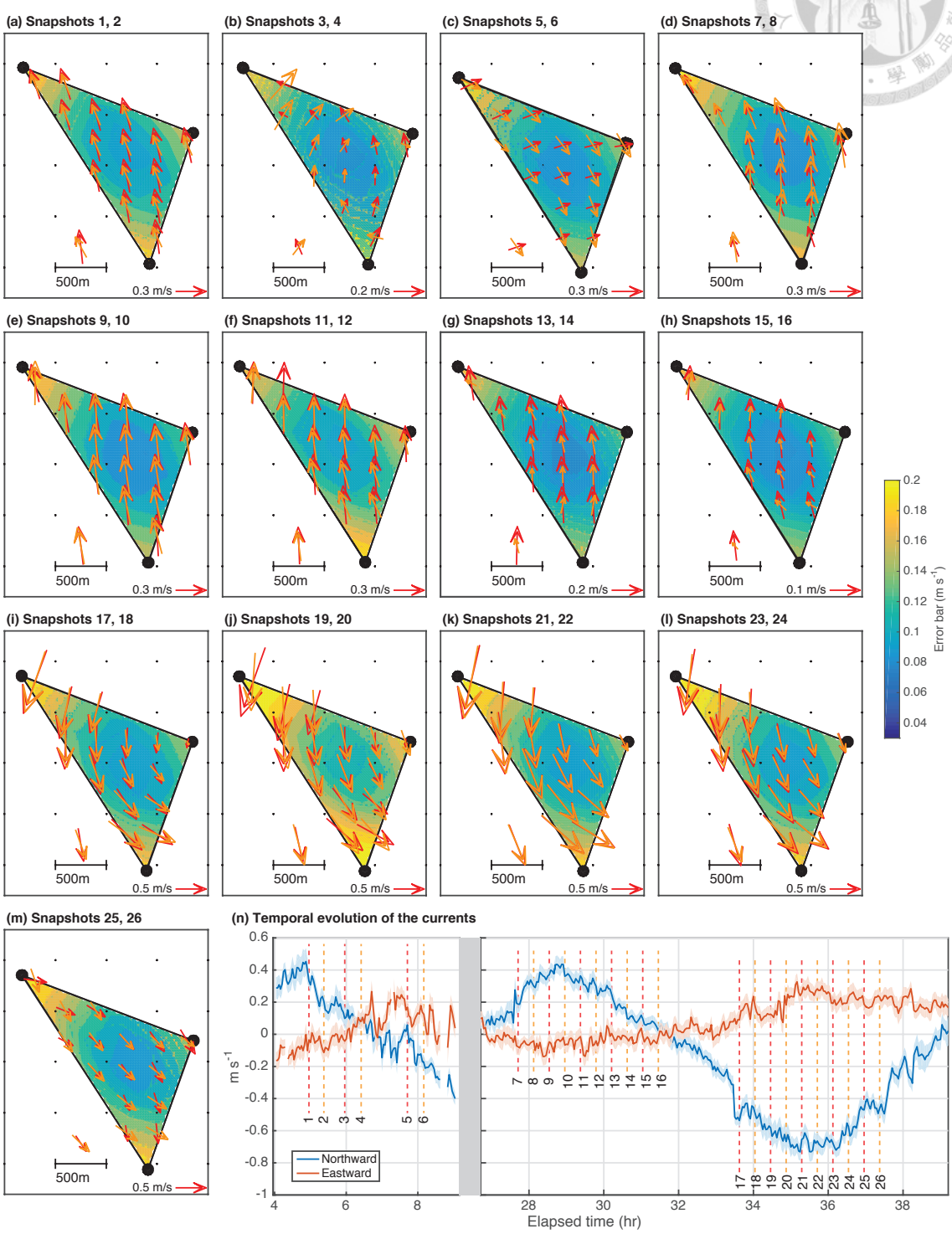

Figure 5.7: (a)–(m) Snapshots of the estimated current fields. (n) Temporal evolution of the currents.

10.6342/NTU201603287

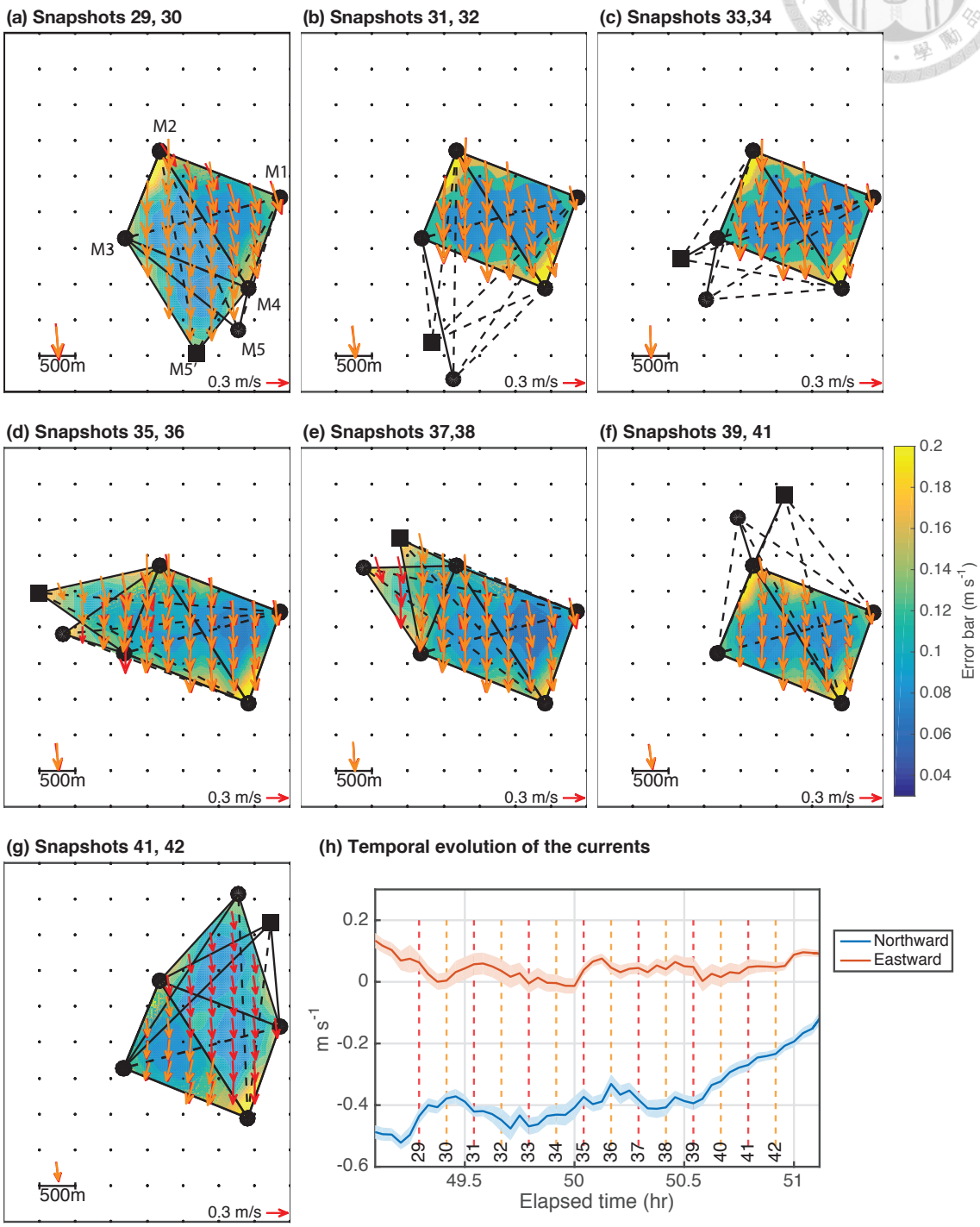

Figure 5.8: (a)–(g) Snapshots of the estimated current fields. (h) Temporal evolution of the currents.

10.6342/NTU201603287

5.3 Validation of the Estimated Current Field

The estimated current field was validated using the DTT data of the ray paths not included in estimating the currents. Figure 5.9 shows a spatial distribution of the estimated current field using the rays indicated by the black solid lines. The dashed line indicates the path of no acoustic reception. Since the ray colored in red is not included in the current estimation, the observed DTT value (Δt_{obs}) is used to compare with the predicted DTT (Δt_{pre}) from the estimated current. The predicted DTT Δt_{pre} along with its error bar $\sigma_{\Delta t_{\text{pre}}}$ are derived from the estimated field and the geometry of the stations. The calculation involves the path integral of the current velocity along the ray path (as shown in red line). Ideally, the observed and the predicted DTTs should be close, i.e., $\Delta t_{\text{obs}} = \Delta t_{\text{pre}}$. A high DTT residual ($|\Delta t_{\text{obs}} - \Delta t_{\text{pre}}|$) compared to their uncertainties $\sigma_{\Delta t_{\text{pre}}}$ and $\sigma_{\Delta t_{\text{obs}}}$ may suggest the estimated current is incorrect.

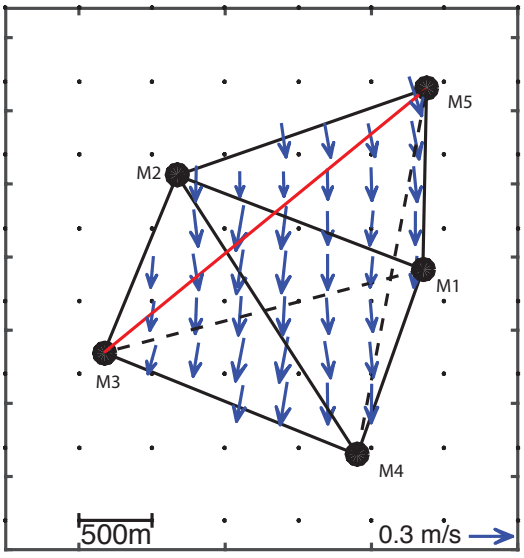

Figure 5.9: An example of the estimated current field.

In this experiment, 56 redundant DTTs are used to validate of the estimated current field. The histogram of the DTT residuals $|\Delta t_{\text{obs}} - \Delta t_{\text{pre}}|$ is shown in Figure 5.10(a). Considering $\sigma_{\Delta t_{\text{pre}}}$ and $\sigma_{\Delta t_{\text{obs}}}$, the error bar for the residual is given by $\sqrt{\sigma^2_{\Delta t_{\text{obs}}} + \sigma^2_{\Delta t_{\text{pre}}}}$.

Figure 5.10(b) shows the histogram for the ratio of the DTT residual to its error bar. About 90% of the residuals is below its error bar. This means that the redundant data agree with the estimated current fields.

10.6342/NTU201603287

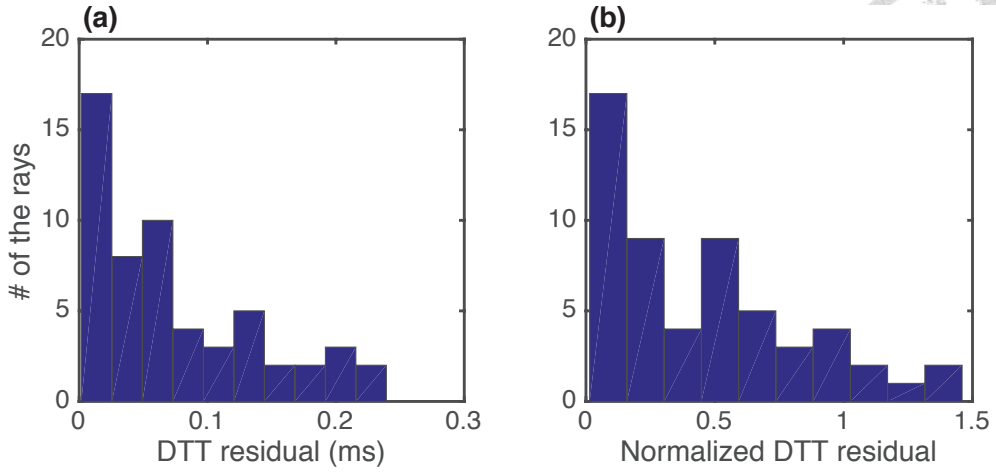

Figure 5.10: Distribution of (a) the residual DTT $|\Delta t_{\text{obs}} - \Delta t_{\text{pre}}|$ and (b) the ratio of the residual DTT to its error bar.

5.4 Error Analysis

An error analysis of the estimated current is carried out using the relation obtained in Section 2.1 [Equation (2.4)]

$$v_{\text{m}} = -\frac{c^2 \Delta t_{12}}{2R} - \frac{u_{\text{r}}}{2}, \tag{5.1}$$

The uncertainties in the sound speed c, the distance between Stations 1–2, R, the DTT Δt_{12}, and the velocity of the towed station u_{r} will propagate to the uncertainty in the estimate v_{m}. Note that one may not compare v_{m} with the point-measurement velocity directly because the former represents the averaged velocity along the ray path. Therefore, the uncertainty in v_{m} is investigated from the uncertainties in the parameters on the right-hand side of Equation (5.1).

Among all the parameters, the uncertainties in c and R are relatively small. The measured sound speeds at different times and spaces varied from 1537 to 1542 $\text{m}\,\text{s}^{-1}$. For the reference sound speed of 1540 $\text{m}\,\text{s}^{-1}$, the fractional error of c is in the order of 10^{-3}. The distance R is more than 1.3 km between the moored stations and varies from about 0.7 km to 3.5 km between the moored and towed stations. The distances were estimated using the GPS positions measured at each acoustic transmission. Considering the error in the GPS measurement, a conservative estimate of the fractional error of R is in the order of 10^{-2}.

The uncertainty in the DTT, $\sigma_{\Delta t_{12}}$, has the fraction error in the order of 10^{-1}, which is the main source of the uncertainty in v_{m}. The uncertainty $\sigma_{\Delta t_{12}}$ is estimated using the root-mean-square deviation (RMSD) between the original (Δt_{12})

10.6342/NTU201603287

and filtered $\left(\widehat{\Delta t}_{12}\right)$ DTT measurements:

$$\sigma_{\Delta t_{12}} = \sqrt{\frac{1}{M}\sum_{k=1}^{M}(\Delta t_{12,k} - \widehat{\Delta t}_{12,k})^2}, \tag{5.2}$$

where $\Delta t_{12,k}$ denotes the DTT obtained at the kth transmission and $\widehat{\Delta t}_{12,k}$ is the filtered DTT obtained by a 11-point moving average:

$$\widehat{\Delta t}_{12,k} = \frac{1}{11}\sum_{p=k-5}^{k+5}\Delta t_{12,p}. \tag{5.3}$$

We found that the uncertainty $\sigma_{\Delta t_{12}}$ is less than 0.1 ms in this study. The DTT typically varied from -1 to 1 ms, and thus the fraction error is in the order of 10^{-1}.

The precision of the travel-time measurements is a complicated topic. The precision in this study is limited by the ambient noise and the ray interference, where the latter may be the dominant factor but lack for theoretical analysis. For the ambient noise, the RMS error of the travel time is given by [6]

$$\sigma_t = \frac{1}{2\pi B_{\text{rms}}}\sqrt{\frac{N_0}{E}}, \tag{5.4}$$

where B_{rms} is the RMS bandwidth of the transmitted signal in Hertz. The assumption for Equation (5.4) is that the ambient noise is an additive Gaussian noise with a flat spectrum in the frequency band of the acoustic transmission and the SNR of the signal is large. In this study, the bandwidth B_{rms} is about 2.1 kHz, resulting in σ_t of about 10^{-5} s for the signal with the SNR of 15 dB. However, the dominant factor for obtaining a precise travel time is the ray interference. The ray interference is the interference between the closely arriving rays in the acoustic data, which leads to the difficulties in obtaining precise times of the individual arrival peaks. It is also difficult to quantify the uncertainty in the measured travel time induced by the interference.

The uncertainty in the transceiver velocity u_{r} is estimated based on a theoretical analysis. The wideband delay-Doppler ambiguity function for the m-sequence exhibits a symmetric ellipse [Figure 2.8(a)] and there is no coupling between the delay-time and Doppler quantities. In case of large SNR, the uncertainty of the Doppler estimate ($\delta = \Delta f / f_{\text{c}}$) can be approximated by [6]

$$\sigma_\delta \simeq \frac{\sqrt{12}}{2\pi f_{\text{c}} T}\sqrt{\frac{N_0}{E}} \tag{5.5}$$

where E is the received signal energy, N_0 is the average noise power, i.e., E/N_0 denotes the signal-to-noise ratio (SNR) of the matched filter output, and T is the

10.6342/NTU201603287

signal duration. Thus, the uncertainty in u_r is

$$\sigma_{u_\mathrm{r}} = \sigma_\delta \, c, \tag{5.6}$$

where the uncertainty in c is neglected for its small uncertainty (a fractional error in the order of 10^{-3}). For the received signal with the SNR of 15 dB, the uncertainty σ_{u_r} is about 3.7 $\mathrm{cm\,s^{-1}}$.

Using the error propagation formula the uncertainty in v_m is derived as

$$\sigma_{v_\mathrm{m}} = \sqrt{\left(\frac{c^2}{2R}\sigma_{\Delta t_{12}}\right)^2 + \left(\frac{\sigma_{u_2}}{2}\right)^2}, \tag{5.7}$$

where the uncertainties in c and R are excluded from the analysis because their small fractional error compared with that in Δt_{12}.

Two scenarios are discussed for the acoustic transmission between 1.5 km distance: (1) the ray between two moored stations, in which u_r is neglected, and (2) the ray between a moored and a towed station, in which u_r is included. Using $\sigma_{\Delta t_{12}}$ of 0.1 ms and σ_{u_r} of 3.7 $\mathrm{cm\,s^{-1}}$, we found that the uncertainties in v_m are 7.9 $\mathrm{cm\,s^{-1}}$ and 8.1 $\mathrm{cm\,s^{-1}}$ for (1) and (2), respectively.

5.5 Summary

We have analyzed the current field using the DTT data obtained from the previous chapter. According to the eigenray simulations, the dominant rays cycle through the entire water column, indicating that the estimated currents using the travel-time measurements are the averaged current over the depth from the surface to the bottom. The DTT obtained from the analysis carried out in Chapter 4 were used to estimate in the currents. The time series of the estimated currents not only reveals the temporal variation of the semi-diurnal tidal currents but also exhibits a consistency with the direct measured current velocity using the shipboard-ADCP. The spatial distribution of the estimated currents is usually small. However, a relatively high spatial variation is observed when the currents change the direction. Incorporation of the towed station increases the number of the ray paths for the current estimate. Some of the data between the towed and moored stations are used to validate for the reconstructed current field.

10.6342/NTU201603287

Chapter 6

Conclusions

6.1 Conclusions

This study analyzed the data collected from the moving vehicle tomography experiment conducted near the Sizihwan Bay in Kaohsiung, Taiwan. Four moored stations and one mobile station were deployed from August 29 to September 2, 2015. The currents in the experiment site were estimated using the acoustic mapping based on the reciprocal travel-time measurements. The basic principle of the currents mapping is that the differential travel time (DTT) of an acoustic pulse traveling in reciprocal directions is linearly proportional to the path-averaged current velocity. Therefore, the ocean currents can be estimated with the DTT data from the reciprocal acoustic transmissions between pairs of the stations.

The field experiment featured a mobile transceiver towed by the research vessel, which effectively increased the quantity of data. The acoustic ray paths between the towed and moored transceivers travel through the ocean from various angles and can potentially improve the current estimation. Two issues related to the towed transceiver were addressed: 1) the received signals were distorted by the Doppler effect, and 2) the velocity of the instrument should be estimated to remove the effect of transceiver motions on the DTT. We used the wideband delay-Doppler ambiguity function of the received signals to address these issues. The computation of the ambiguity function involved cross-correlating the received signals with different Doppler-shifted replicas of the transmitted signal. From the ambiguity function, the acoustic arrivals were revealed, and the relative velocity between the transceiver pair was estimated. The DTT offset due to the transceiver motions was then compensated.

One of the challenging tasks of the data analysis was to obtain the DTT from

10.6342/NTU201603287

the reciprocal arrival patterns. Due to the ray interference, it was difficult to resolve the precise travel time of individual arrivals. The conventional approach for estimating the DTT, the peak-picking method, was difficult to apply: the selection of reciprocal peaks in the arrival patterns is usually manual and is subject to the picking error when multiple arrivals are present closely in the time axis. An alternative approach for the DTT determination is the waveform-matching method, where the DTT is estimated by the lag time at which the cross-correlation function (CCF) between reciprocal patterns reaches the maximum. The method can mitigate the problem occurred in the peak-picking method. However, the CCF usually exhibited multiple peaks with similar magnitudes due to the multiple arrivals and the lag time of the maximum sometimes resulted in incorrect estimates of the DTT. Therefore, we selected the peaks that were consistent with the time-variation pattern of the CCFs for the DTT estimation.

The estimated currents agreed well with the direct measurements. The experiment site was dominant by the semi-diurnal tidal currents with the principal axis parallel to the isobaths. The temporal and spatial variations of the currents were separately estimated using the travel-time based acoustic mapping. The estimated currents were the averaged current over the depth from the surface to bottom as indicated by the eigenray simulations. The temporal evolution of the estimated currents was consistent with the direct measurement from the shipboard-ADCP. The results also revealed the temporal patterns of the tidal currents. From the estimated current fields, we found that the spatial variation of the currents was usually small except when the tidal currents changed its direction. The estimated fields were also validated by some of the data between the towed and moored stations.

6.2 Suggestions of Further Development

Suggestions for future research are listed below:

- Matched-Field Inversion
  In the acoustic mapping, only the (differential) travel time was extracted from the acoustic data for estimating the currents. There are other approaches such as the full-wave inversion or the matched-field inversion that, instead of using the travel-time data of the acoustic data, incorporate the entire waveform for the analysis. These methods generate the modeled fields using a sophisticated modeling of the sound channel. The parameters (not limited to the current velocity) along with their uncertainties of the environment can then be estimated

10.6342/NTU201603287

by matched filtering the modeled fields with the measured field.

- The algorithm for current reconstruction
  In the present algorithm of the current reconstruction, the current field is independently estimated at each time. From the previous survey [35], the experiment area is dominant by the semi-diurnal tidal currents. It may be possible to improve the results of the acoustic mapping by incorporating the knowledge regarding to the temporal evolution of the ocean currents, which could be gained from the ocean models or the climatological data.

10.6342/NTU201603287

Appendix A

This appendix is a reprint of the material as it appears in Yun-Wen Li and Chen-Fen Huang, "Shallow-Water Acoustic Tomography of Ocean Currents Using a Moving Ship," In proceeding of the 18th Conference on UnderSea Technology, Tainan, Taiwan, May 2016.

10.6342/NTU201603287

Shallow-Water Acoustic Tomography of Ocean Currents Using a Moving Ship

Yun-Wen Li* and Chen-Fen Huang†

ABSTRACT

This study uses four moored stations along with one towed by a ship to demonstrate moving ship tomography of ocean currents in a shallow water environment. The basic principle of current tomography is that the difference in the travel times (DTT) of oppositely traveling acoustic signals is proportional to the integrated current between the acoustic transceivers. Due to the interference of multipath arrivals in shallow water environments, the cross-correlation function (CCF) of the reciprocal arrival patterns usually exists multiple peaks with a relatively low correlation coefficient. Thus, this study devises a method utilizing the time evolution of the CCFs to select appropriate peaks for the determination of DTT. For the data collected from the towed station, its relative motion also affects the DTT. The relative velocity between the stations is estimated by the method of the delay-Doppler ambiguity function. The acoustic arrival patterns are obtained after compensating the Doppler shift. The methods are applied to the data collected during the feasibility test conducted at Sizhiwan Marine Test Field, in September of 2015. The estimated currents agree with those derived from the shipboard-ADCP measurements.

淺海環境之移動船聲層析測流研究

李允文 [1] 黃千芬 [2]

摘要

本研究在淺海環境下使用四個固定式測站和一個拖曳式測站，實現移動載具水聲層析測流的技術。水聲層析測流的基本原理是利用聲波在一測線上來回走時差與沿著聲線的流場積分成正比。由於水聲通道多重路徑的效應，來回訊號的交互相關函數經常存在多個峰值且其相關係數往往較低，本研究利用相關函數的時間序列，以選擇合適的峰值來估算來回走時差。另，若使用拖曳式測站，其運動亦影響來回走時差；利用發射訊號（M 序列）於匹配訊號處理對頻率變化的敏感度，其測站間的相對速度可由“時間延遲-都卜勒模糊函數”來估計。藉由 2015 年 9 月在西子灣海洋實驗場蒐集的資料，分析結果顯示估算的流場分布與船載式都普勒流速剖面儀的結果一致。

I. INTRODUCTION

Ocean acoustic tomography (OAT) is a measurement technique to obtain the interior ocean properties such as temperature and current fields using the acoustic method.[6] The advantage of OAT is that the travel times of acoustic signals propagating between the sources and receivers provide the integral measures of the ocean, such as heat content, mass transport, and circulation.

Moving Ship Tomography (MST) is a method of obtaining high-resolution, nearly synoptic maps of the ocean temperature or current field over large areas.

*Master student, Institute of Oceanography, National Taiwan University
†Associate Professor, Institute of Oceanography, National Taiwan University

10.6342/NTU201603287

In general, the performance of the current estimate can be improved with more rays (in the properly designed array geometry), which could be achieved with more transceivers. Cornuelle *et al.*[3] proposed to incorporate a ship towing an acoustic transceiver. The rays between ship-towed and moored transceivers pass through the ocean at various angles.

The moving ship tomography has not been conducted in coastal ocean. In this study, we demonstrate the feasibility of the technique by the field experiment. Since the accurate positions of the transceivers were not available, the focus is on the current tomography.

II. EXPERIMENT

The experiment was conducted at Sizhiwan Marine Test Field in September of 2015. The experiment site was located in a shallow-water environment, with the depth varying from 20 to 26 m. Four bottom-moored (M1 to M4) and one ship-towed (M5) stations were deployed to measure the travel times between the stations.

Each station transmitted a separately phase-encoded linear maximum shift-register sequence (m-sequence) with the carrier frequency of 17.986 kHz. All the stations simultaneously transmit the signals with the repetition rate of 30 s and then switch to the reception mode to receive the signals from the remote stations.

III. THEORY

A. The path-averaged current speed and differential travel time

Assuming uniform current velocity ($\mathbf{v}$) in an ocean environment with a reference sound-speed of c, one stationary station i and one towed station j, separated by the distance of L, transmit acoustic pulses reciprocally. The path-averaged current $\mathbf{v}\cdot\mathbf{n}_{ij}$ can be expressed by:

$$\mathbf{v}\cdot\mathbf{n}_{ij} = -\frac{c^2\Delta t_{ij}}{2L} - \frac{1}{2}u_{\mathrm{r}}, \qquad (1)$$

where $\mathbf{n}_{ij}$ is the unit vector of $i \to j$ direction, $\Delta t_{ij} = t_{ij} - t_{ji}$ is the DTT, in which t_{ij} is the travel time of the $i \to j$ propagating signal, and u_{r} is the the radial (in the axis of propagating path) velocity of station j relative to station i, which is positive when the stations get closer.

IV. DATA ANALYSIS

A. DTT estimate

Before estimating the DTT, the reciprocal arrival patterns are computed. Assuming the acoustic signals are Doppler affected, the Doppler factor of a received signal is estimated using the delay-Doppler ambiguity function.[5] The received signal is then matched-filtered by the Doppler-shifted replica of the transmitted signal to obtain the arrival pattern.

Due to complicated propagation characteristics in the underwater channel, it is difficult to pick up paired arrivals in the reciprocal patterns and to apply the peak-picking method[2]. The difficulty can be mitigated using the waveform-matching method. Its limitation is that the DTTs for individual arrivals are not available. For the waveform-matching method, one calculates the cross-correlation function (CCF) between reciprocal arrival patterns. Ideally, the reciprocal arrivals have similar patterns with slightly different arrival times, resulting from the current effect. The DTT is estimated by the lag time of the maximum in the CCF. However, the maximum could sometimes lead to the incorrect estimate of DTTs.

Figure 1 shows an example of (a) reciprocal patterns and (b) the resulting CCF from the measured data. In Fig. 1(a), the red pattern denotes the signal of M2→M1 direction while the blue one denotes that of the opposite di-

10.6342/NTU201603287

rection. Each pattern has high SNR (higher than 20 dB) and is normalized. Two pairs of reciprocal arrivals, R1-B1 and R2-B2 pair, are identified. Note that the magnitude of R1 is far smaller than that of B1.

In Fig.1(b), the CCFs have multiple peaks due to the multiple arrivals, and each peak is the result of the alignment of peaks in reciprocal patterns and is denoted by a number. The highest peak (peak 4) corresponds to the alignment of R2-B1 pair instead of the R1-B1 and R2-B2 pairs. Thus, a reasonable estimate of DTT should consider all potential peaks in the CCF and select the one which is persistently present over time. We select the peaks based on the time-evolution of the CCFs as shown in Fig. 1(c). Each CCF (each horizontal slice in the figure) is averaged over 5 adjacent CCFs and then normalized by the maximum. The average process reduces random fluctuations and enhances the trend of the peaks in CCFs. The black cross symbol indicates the maximum peak in the CCF prior to the average and the white circle is the predicted DTT calculated based on the current velocity measured by the Shipboard-ADCP. We see that the lag time of the maximum peaks agrees well with the predicted DTT, except for the peaks inside the white rectangles. The trend of those peaks is inconsistent with that of the rest peaks due to the reason discussed in Fig. 1(b). The time-evolution of the CCFs can be used to track the appropriate peaks for the determination of DTT.

B. Current estimation

The spatial and temporal variation of the ocean current are discussed separately. To estimate the spatial variation, we apply the method proposed by Huang *et al.*[4] to reconstruct the current field. To estimate the temporal variation, we assume a uniform current $\mathbf{v}$. The current $\mathbf{v}$ can be estimated using Eq. (1). Combining data from multiple rays, the measurements are related to current $\mathbf{v}$ in a matrix form $\mathbf{d} = \mathbf{G}\mathbf{v}$, where $\mathbf{v}$ is the current vector (northward and the eastward current components) and $\mathbf{d}$ is the data vector. Each element in $\mathbf{d}$ is the right-hand side of Eq. (1), which includes the DTT Δt_{ij} and the motion of the towed station u_{r}. The procedure to estimate the Δt_{ij} is described in IV.A and u_{r} is estimated by the Doppler factor of the signal.[5] The kth row in $\mathbf{G}$ is the unit vector along the ray corresponding to the kth element in $\mathbf{d}$. The $\mathbf{v}$ can be estimated by conventional least square method, which minimizes $||\mathbf{d} - \mathbf{G}\mathbf{v}||$.

V. RESULTS

Figure 2 shows the estimated current velocity in (a) eastward and (b) northward directions (blue line) with their corresponding error bars (light blue area). The black circle indicates the *in situ* current derived from the shipboard-ADCP measurement. Each snapshot of the current estimate is obtained by a 11th order median filter. The time interval between the adjacent estimates is 2 min.

The time series of estimated current captures the evolution of four tidal cycles, and the trend of the estimate is consistent with the current derived from the ADCP. Note that these two current estimates are different: the current obtained from the tomography technique is the path-averaged current along the ray path, whereas the current derived from the shipboard-ADCP is the point-measured current at the ship position.

Figure 2(c) shows several snapshots of the estimated current fields. The line indicates the ray path, the arrow symbol is the estimated current vector, and the circle is the station. The current is strong in the along-shore direction with the maximum magnitude of about 0.65 m/s and is weak in the cross-shore direction with the maximum magnitude of about

10.6342/NTU201603287

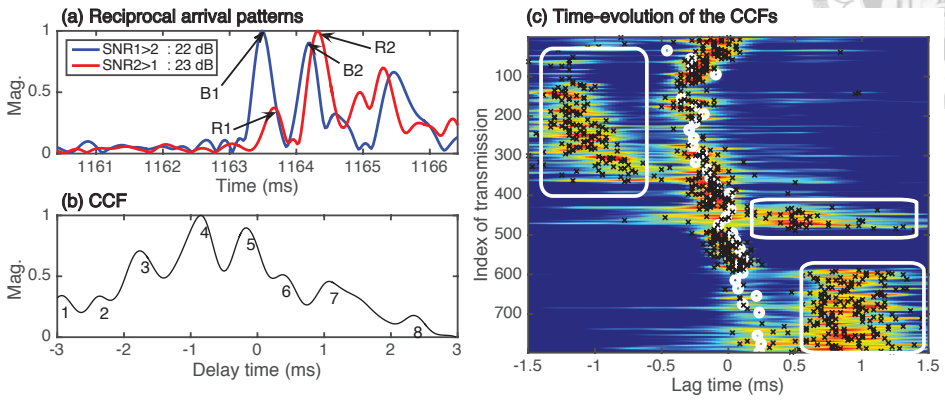

FIG. 1. (a) Reciprocal arrival patterns. (b) The CCF. The number indicates the peak in the CCF. (c) Time-evolution of the CCF. The data are from reciprocal transmission between M1 and M2. The transmission began at 16:21 on August 30, 2015 (local time) with the transmission interval of 30 s.

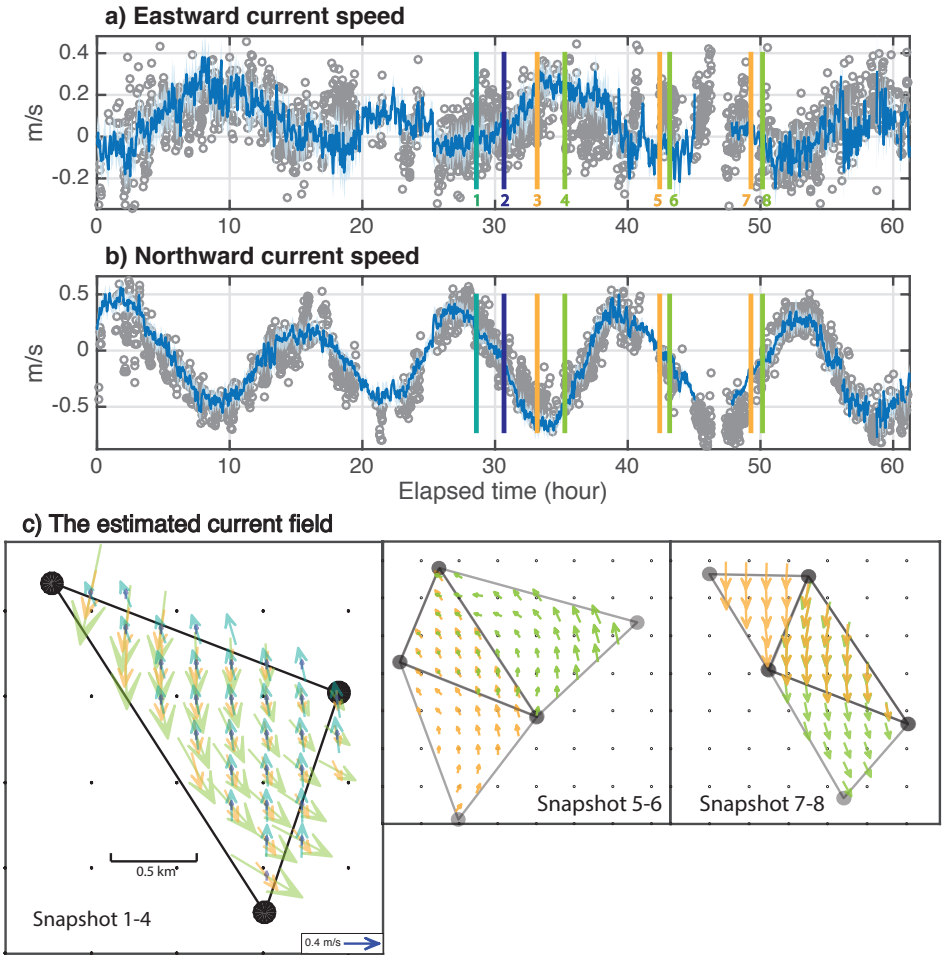

FIG. 2. Time-series of the estimated current in (a) northward and (b) eastward directions, which began at 15:01 on August 29, 2015. (c) Snapshots of estimated current fields.

10.6342/NTU201603287

0.18 m/s. The spatial variation of the current is usually small. When the tidal currents change direction, there is more spatial variation of currents, as shown in Snapshots 3 and 4. We see that during these times the cross-shore current in the south area is stronger than that in the north.

VI. SUMMARY

This study analyzed the data taken from the moving ship tomography experiment conducted at Sizhiwan Marine Test Field, Kaohsiung. With the ship-towed station, the acoustic ray path between the towed and moored stations can sample the ocean from different angles and potentially improves the current estimation. Based on the delay-Doppler ambiguity function, the Doppler factors of the Doppler-affected acoustic signals could be estimated. Using the estimated Doppler factors, the relative motion of the instrument can be estimated and the distinct acoustic arrivals are revealed using the Doppler-adjusted matched-filter. Due to the interference of multi-path arrivals, it is difficult to estimate the DTTs from reciprocal arrival patterns. The modified waveform-matching method is applied with incorporation of the time-evolution of the CCFs.

The temporal variation and the spatial distribution of the current are estimated from the obtained DTTs. The temporal variation of the estimated current is consistent with the point-measurement derived from the shipboard-ADCP. The estimated spatial field captures the current structure when the tidal currents change direction.

[1] Moving ship tomography in the north atlantic. *Eos, Transactions American Geophysical Union 75*, 2 (1994), 17–23.

[2] Chen, Y. H., Taniguchi, N., Liu, C. T., and Huang, C. F. Acoustic current measurement using travel-time method in bachimen harbor, taiwan. In *OCEANS 2014 - TAIPEI* (April 2014), pp. 1–5.

[3] Cornuelle, B., Munk, W., and Worcester, P. Ocean acoustic tomography from ships. *Journal of Geophysical Research: Oceans 94*, C5 (1989), 6232–6250.

[4] Huang, C.-F., Yang, T. C., Liu, J.-Y., and Schindall, J. Acoustic mapping of ocean currents using networked distributed sensors. *The Journal of the Acoustical Society of America 134*, 3 (2013), 2090–2105.

[5] Jourdain, G., and Henrioux, J. P. Use of large bandwidth-duration binary phase shift keying signals in target delay Doppler measurements. *J. Acoust. Soc. Am. 90*, 1 (1991), 299–309.

[6] Munk, W., Worcester, P., and Wunsch, C. *Ocean Acoustic Tomography*. Cambridge University Press, 1995.

10.6342/NTU201603287

Bibliography

[1] D. Behringer, T. Birdsall, M. Brown, B. Cornuelle, R. Heinmiller, R. Knox, K. Metzger, W. Munk, J. Spiesberger, R. Spindel, D. Webb, P. Worcester, and C. Wunsch. A demonstration of ocean acoustic tomography. *Nature*, 299:121–125, 1982.

[2] Y.-H. Chen, N. Taniguchi, C.-T. Liu, and C.-F. Huang. Acoustic current measurement using travel-time method in Bachimen Harbor, Taiwan. In *OCEANS 2014 - TAIPEI*, pages 1–5, 2014.

[3] B. Cornuelle, W. Munk, and P. Worcester. Ocean acoustic tomography from ships. *J. Geophys. Res.: Oceans*, 94(C5):6232–6250, 1989.

[4] Cypress Semiconductor. *PSoC® 5LP: CY8C58LP family datasheet: Programmable system-on-chip (PSoC®).*

[5] V. A. Del Grosso. New equation for the speed of sound in natural waters (with comparisons to other equations). *J. Acoust. Soc. Am.*, 56(4):1084–1091, 1974.

[6] Y. Doisy, L. Deruaz, S. Beerens, and R. Been. Target Doppler estimation using wideband frequency modulated signals. *IEEE Trans. Signal Process.*, 48(5):1213 –1224, may 2000.

[7] S. Haykin. *Communication systems.* John Wiley & Sons, 2008.

[8] C.-F. Huang. Moving vehicle tomography using distributed networked underwater sensors. Report for the research program supported by Ministry of Science and Technology, R. O. C., Institute of Oceanography, National Taiwan University, 2016.

[9] C.-F. Huang, N. Taniguchi, Y.-H. Chen, and J.-Y. Liu. Estimating temperature and current using a pair of transceivers in a harbor environment. *J. Acoust. Soc. Am.*, 140(1):EL137–EL142, 2016.

10.6342/NTU201603287

[10] C.-F. Huang, T. C. Yang, J.-Y. Liu, and J. Schindall. Acoustic mapping of ocean currents using networked distributed sensors. *J. Acoust. Soc. Am.*, 134(3):2090–2105, 2013.

[11] G. Jourdain and J. P. Henrioux. Use of large bandwidth-duration binary phase shift keying signals in target delay Doppler measurements. *J. Acoust. Soc. Am.*, 90(1):299–309, 1991.

[12] D. S. Ko, H. A. DeFerrari, and P. Malanotte-Rizzoli. Acoustic tomography in the Florida Strait: Temperature, current, and vorticity measurements. *J. Geophys. Res.: Oceans*, 94(C5):6197–6211, 1989.

[13] T. J. McDougall and P. M. Barker. Getting started with TEOS—10 and the Gibbs Seawater (GSW) Oceanographic Toolbox. *SCOR/IAPSO WG127*, 2011.

[14] T. J. McDougall, D. R. Jackett, F. J. Millero, R. Pawlowicz, and P. M. Barker. A global algorithm for estimating Absolute Salinity. *Ocean Sci.*, 8(6):1123–1134, 2012.

[15] W. Munk, P. Worcester, and C. Wunsch. *Ocean acoustic tomography*. Cambridge University Press, 1995.

[16] W. Munk and C. Wunsch. Ocean acoustic tomography: A scheme for large scale monitoring. *Deep-Sea Res., Part A*, 26(2):123 – 161, 1979.

[17] W. H. Munk, R. C. Spindel, A. Baggeroer, and T. G. Birdsall. The Heard Island feasibility test. *J. Acoust. Soc. Am.*, 96(4):2330–2342, 1994.

[18] Neptune Sonar Limited. *The datasheet of model T235 transducer*.

[19] Nortek AS. *Aquadopp Profiler brochure*.

[20] S. J. Norton. Tomographic reconstruction of 2-D vector fields: Application to flow imaging. *Geophys. J. Int.*, 97(1):161–168, 1989.

[21] Ocean Data Bank of the Ministry of Science and Technology, Republic of China. Bathymetric data around Taiwan. http://www.odb.ntu.edu.tw/.

[22] M. B. Porter. Acoustics toolbox. http://oalib.hlsresearch.com/.

[23] M. B. Porter and H. P. Bucker. Gaussian beam tracing for computing ocean acoustic fields. *J. Acoust. Soc. Am.*, 82(4):1349–1359, 1987.

10.6342/NTU201603287

[24] H. Preston-Thomas. The international temperature scale of 1990 (ITS-90). *Metrologia*, 27(1):3, 1990.

[25] Sea-Bird Electronics. *SBE 9plus manual*.

[26] N. Taniguchi, C.-F. Huang, A. Kaneko, C.-T. Liu, B. M. Howe, Y.-H. Wang, Y. Yang, J. Lin, X.-H. Zhu, and N. Gohda. Measuring the Kuroshio Current with ocean acoustic tomography. *J. Acoust. Soc. Am.*, 134(4):3272–3281, 2013.

[27] Teledyne RD Instruments. *Ocean Surveyor ADCP datasheet*.

[28] The Acoustic Mid-Ocean Dynamics Experiment Group. Moving ship tomography in the North Atlantic. *Eos Trans. AGU*, 75(2):17–23, 1994.

[29] U-blox. *NEO-6T / LEA-6T product summary*.

[30] UNESCO. The practical salinity scale 1978 and the international equation of state of seawater 1980. Technical Report 36, UNESCO Technical Paper in Marine Science, 1981.

[31] J. Valladares, W. Fennel, and E. Morozov. Replacement of EOS-80 with the International Thermodynamic Equation of Seawater - 2010 (TEOS-10). *Deep-Sea Res., Part I*, 58(9):978, 2011.

[32] L. G. Weiss. Wavelets and wideband correlation processing. *IEEE Signal Proc. Mag.*, 11(1):13–32, 1994.

[33] E. W. Weisstein. Cross-Correlation. MathWorld–A Wolfram Web Resource. http://mathworld.wolfram.com/Cross-Correlation.html.

[34] P. F. Worcester. Reciprocal acoustic transmission in a midocean environment. *J. Acoust. Soc. Am.*, 62(4):895–905, 1977.

[35] M.-H. Xiao. A very shallow water acoustic propagation experiment in the Si-Tzi Marine Test Field. Master thesis, Institute of Undersea Technology, National Sun Yat-Sen University, 2009.

[36] K. Yamaguchi, J. Lin, A. Kaneko, T. Yayamoto, N. Gohda, H.-Q. Nguyen, and H. Zheng. A continuous mapping of tidal current structures in the Kanmon Strait. *J. Oceanogr.*, 61(2):283–294, 2005.

[37] H. Yamoaka, A. Kaneko, J.-H. Park, H. Zheng, N. Gohda, T. Takano, X.-H. Zhu, and Y. Takasugi. Coastal acoustic tomography system and its field application. *IEEE J. Oceanic Eng.*, 27(2):283–295, 2002.

10.6342/NTU201603287

[38] H. Zheng, N. Gohda, H. Noguchi, T. Ito, H. Yamaoka, T. Tamura, Y. Takasugi, and A. Kaneko. Reciprocal sound transmission experiment for current measurement in the Seto Inland Sea, Japan. *J. Oceanogr.*, 53:117–127, 1997.

[39] X. H. Zhu, A. Kaneko, Q. Wu, C. Zhang, N. Taniguchi, and N. Gohda. Mapping tidal current structures in Zhitouyang Bay, China, using coastal acoustic tomography. *IEEE J. Oceanic Eng.*, 38(2):285–296, 2013.

[40] 劉金源，《水中聲學 – 水聲系統之基本原理操作》，國立編譯館，2001。

10.6342/NTU201603287